A&A 499, 69–85 (2009)
DOI: 10.1051/0004-6361/200811526

Astronomy & Astrophysics

GMASS ultradeep spectroscopy of galaxies at z ∼ 2

IV. The variety of dust populations

S. Noll[1,2], D. Pierini[2], A. Cimatti[3], E. Daddi[4], J. D. Kurk[5], M. Bolzonella[6], P. Cassata[7], C. Halliday[8], M. Mignoli[6], L. Pozzetti[6], A. Renzini[9], S. Berta[2], M. Dickinson[10], A. Franceschini[11], G. Rodighiero[11], P. Rosati[12], and G. Zamorani[6]

[1] Observatoire Astronomique de Marseille-Provence, 38 rue Frédéric Joliot-Curie, 13388 Marseille Cedex 13, France
e-mail: stefan.noll@oamp.fr
[2] Max-Planck-Institut für extraterrestrische Physik, Giessenbachstr., 85748 Garching, Germany
[3] Dipartimento di Astronomia, Università di Bologna, via Ranzani 1, 40127 Bologna, Italy
[4] CEA-Saclay, DSM/DAPNIA/Service d'Astrophysique, 91191 Gif-sur-Yvette Cedex, AIM-Unité Mixte de Recherche CEA-CNRS (#7158)-Université Paris VII, France
[5] Max-Planck-Institut für Astronomie, Königstuhl 17, 69117 Heidelberg, Germany
[6] INAF – Osservatorio Astronomico di Bologna, via Ranzani 1, 40127 Bologna, Italy
[7] Department of Astronomy, University of Massachusetts, LGRT-B 619E, 710 North Pleasant Street, Amherst, MA 01003-9305, USA
[8] INAF – Osservatorio Astrofisico di Arcetri, Largo E. Fermi 5, 50125 Firenze, Italy
[9] INAF – Osservatorio Astronomico di Padova, Vicolo dell'Osservatorio 5, 35122 Padova, Italy
[10] NOAO-Tucson, 950 North Cherry Avenue, Tucson, AZ 85719, USA
[11] Università di Padova, Dipartimento di Astronomia, Vicolo dell'Osservatorio 2, 35122 Padova, Italy
[12] European Southern Observatory, Karl-Schwarzschild-Str. 2, 85748 Garching, Germany

Received 15 December 2008 / Accepted 4 March 2009

ABSTRACT

Aims. The properties of dust attenuation at rest-frame UV wavelengths are inferred from very high-quality FORS 2 spectra of 78 galaxies from the GMASS survey at redshift $1 < z < 2.5$. These objects complement a previously investigated sample of 108 UV-luminous, intermediate-mass (i.e., with stellar masses $\sim 10^{10}$–10^{11} $M_\odot$) galaxies at similar redshifts, selected from the FDF spectroscopic survey, the K20 survey, and the GDDS. Detection of the broad absorption feature centred on about 2175 Å ("UV bump") implies that the average UV extinction curve of a galaxy more closely resembles that of the Milky Way (MW) or the Large Magellanic Cloud (LMC), and differs from that of the Small Magellanic Cloud (SMC).

Methods. The shape of the UV extinction curve is constrained by a parametric description of the rest-frame UV continuum with the support of a suite of models combining radiative transfer and stellar population synthesis. The UV bump is further characterised by fitting Lorentzian-like profiles.

Results. Spectra exhibit a significant 2175 Å feature in at least 30% of the cases, especially those suffering from substantial reddening. If attenuation is dominated by dust ejected from the galaxy main body via galactic winds or more localised superwinds, UV extinction curves in-between those of the SMC and LMC characterise UV-luminous, intermediate-mass galaxies at $1 < z < 2.5$. The fraction of galaxies with extinction curves differing from the SMC one increases, if more dust resides in the galactic plane or dust attenuation depends on stellar age. On average, the width of the manifested UV bumps is about 60% of the values typically measured along sightlines in the LMC and MW. This suggests the presence of dust similar to that found in the "supergiant" shell of ionised filaments LMC 2, close to 30 Dor. The presence of the carriers of the UV bump (probably organic carbon and amorphous silicates) at $1 < z < 2.5$ argues for outflows from asymptotic giant branch (AGB) stars being copious then. Consistent with their higher star-formation rates, the GMASS galaxies with a manifested UV bump are more luminous at rest-frame 8 μm, where the emission is dominated by polycyclic aromatic hydrocarbons (also products of AGB stars). In addition, they exhibit larger equivalent widths for prominent UV (metal) absorption features, mostly of interstellar origin, which indicates overall more evolved stellar populations.

Conclusions. We conclude that diversification of the small-size dust component (responsible for the differential extinction at UV wavelengths and the emission at mid-IR wavelengths) has already started in the most evolved star-forming systems at $1 < z < 2.5$.

Key words. galaxies: high-redshift – galaxies: starburst – galaxies: ISM – ISM: dust, extinction – ultraviolet: galaxies

1. Introduction

A broad absorption excess centred on 2175 Å (the so-called "UV bump") characterises the extinction curves usually inferred for sightlines towards the Milky Way (MW) and Large Magellanic Cloud (LMC) (for reviews see Fitzpatrick 2004; and Clayton 2004), and also towards M 31 (Bianchi et al. 1996). In contrast, this feature is absent in the typical extinction curves of the Small Magellanic Cloud (SMC), which exhibit a steep rise at far-UV wavelengths. SMC-like dust appears to characterise starburst galaxies in the local Universe (Calzetti et al. 1994) and Lyman break galaxies (LBGs) at redshifts $2 < z < 4$ (Vijh et al. 2003). For this reason, the so-called "Calzetti law" (Calzetti et al. 1994, 2000) is frequently assumed to describe attenuation by dust in starburst and star-forming galaxies in the distant Universe.

However, there is strong support for the presence of the 2175 Å feature in spectra of at least 30% of the vigorously

star-forming galaxies at $2 < z < 2.5$ (Noll & Pierini NP05, hereafter referred to as NP05) and $1 < z < 1.5$ (Noll et al. NPPS, hereafter referred to as NPPS). Furthermore, an LMC-like extinction curve with a UV bump was inferred clearly from both the spectrum and the broad-band spectral energy distribution (SED) of the afterglow of the gamma ray burst GRB 070802 at $z = 2.45$ (Fynbo et al. 2007; Krühler et al. 2008; Elíasdóttir et al. 2008). As for other objects at intermediate/high redshifts, the presence of the carriers of the 2175 Å feature is controversial in quasars/active galactic nuclei (AGN) (cf. Pitman et al. 2000; Maiolino et al. 2001; Hopkins et al. 2004; Vernet et al. 2001) and intervening Mg II absorbers (Malhotra 1997; Wang et al. 2004; Vanden Berk et al. 2008), whereas it is likely in Ca II absorbers at intermediate redshifts (Wild & Hewett 2005).

It would therefore be important and interesting to understand when the carriers of the UV bump first appeared in the Universe and how they can survive in vigorously star-forming galaxies at high redshifts. Multiple carriers (i.e., organic carbon and amorphous silicates) are likely to explain the almost invariant central wavelength and variable bandwidth of the 2175 Å feature (Bradley et al. 2005, and references therein). However, a random, hydrogen-free assembly of microscopic sp^2 carbon chips, forming a macroscopically homogeneous and isotropic solid, has recently been proposed as a model carrier of the UV bump by Papoular & Papoular (2009). According to this promising model, different grain formation histories and/or different interstellar radiation fields and other heating effects are responsible for a change in bandwidth without notably impacting the central wavelength. Whatever the carrier of the UV bump, the proportions of the interstellar dust ingredients that are responsible for both the UV bump and the far-UV rise in the extinction curve, relative to each other, are approximately similar in both the MW and LMC, but appear to differ significantly in the SMC (Whittet 2003). Differences also exist within the MW for different sightlines and towards different environments, from dense molecular clouds to the diffuse interstellar medium (ISM; see Fitzpatrick 2004). They must reflect the extreme sensitivity of the small-size dust components to the local chemical enrichment and energy budget (in terms of radiation field and shocks), as well as their selective removal from the size distribution due to a number of physical processes (e.g., Whittet 2003; Gordon et al. 2003).

We continue an analysis started by NP05 and extended by NPPS. We adopt a new homogeneous sample of UV-luminous, intermediate-mass galaxies at $1 < z < 2.5$ drawn from the spectroscopic catalogue of the galaxy mass assembly ultradeep spectroscopic survey (GMASS, Kurk et al. 2008a; Cimatti et al. 2008; Kurk et al., in prep.) in the GOODS-South Field (GOODS-S; Giavalisco et al. 2004). This sample has about 70% of the size of the entire sample in NPPS, but contains mostly objects in the poorly investigated range $1.5 < z < 2.0$, known as the "redshift desert". The excellent dataset available for the GMASS sample enables us to characterise more accurately the apparent shape of the 2175 Å feature in high-redshift star-forming galaxies, and to investigate the relation between dust properties inferred from attenuation at UV wavelengths and emission at mid-IR wavelengths. Furthermore, it adds relevant information about the link between small-size dust populations (i.e., large molecules and small grains) and chemical abundances in stars and gas of the host galaxies.

Throughout this paper, we adopt a ΛCDM cosmological model where $\Omega_\Lambda = 0.7$, $\Omega_M = 0.3$, and $H_0 = 70\,\mathrm{km\,s^{-1}\,Mpc^{-1}}$. By default, photometry is given in the Vega magnitude system; otherwise *AB* magnitudes are indicated.

2. The sample

2.1. The GMASS sample

The GMASS spectroscopic catalogue (Kurk et al. 2008a; Kurk et al., in prep.) comprises 167 objects with secure spectroscopic redshifts. It is based on a mass-sensitive selection criterion using photometry in the *Spitzer* 4.5 μm IRAC filter ($m_{AB}(4.5\,\mu\mathrm{m}) < 23$), and the additional photometric-redshift criterion $z_{\mathrm{phot}} > 1.4$. For our analysis, we identify and select vigorously star-forming objects, for which we can robustly describe the continuum emission at rest-frame wavelengths from 1700 to 2600 Å in the parametric way illustrated by NP05 and NPPS (see Sect. 3.1). In the (spectroscopic) redshift range of our interest ($1 < z < 2.5$), GMASS yields a total of 78 class 2 objects, i.e., actively star-forming galaxies with UV spectra dominated by young stellar populations and no AGN features (see Mignoli et al. 2005). For 68 objects spectroscopically confirmed to lie at $1.5 < z < 2.5$, selection biases are understood: the average galaxy is about 0.2–0.25 mag fainter at 4.5 μm ($\langle m_{AB}(4.5\,\mu\mathrm{m})\rangle = 22.0$, $\sigma = 0.7$) than the average objects in the full spectroscopic and photometric samples for $m_{AB}(4.5\,\mu\mathrm{m}) < 23$ and $1.5 < z < 2.5$. Conversely, it is about 0.3 and 0.8 mag brighter in the visual ($\langle V_{606,AB}\rangle = 24.3$, $\sigma = 0.5$) than the average galaxies in these two catalogues, respectively. Therefore, the following analysis addresses almost exclusively the sample of 68 GMASS UV-luminous galaxies at $1.5 < z < 2.5$.

The spectroscopic observations for the GMASS sample were carried out with FORS 2 at the VLT using the blue 300V and the red 300I grisms, at resolutions of 440 and 660, respectively. Only a minority of the objects was observed in both masks. In view of the particularly long exposure times per mask of 11 to 32 h (and consequently high signal-to-noise ratio – S/N), the main reason for rejecting a spectrum is the limited wavelength coverage.

For the GOODS-S, a wealth of multiwavelength data is available as part of the GOODS legacy (Dickinson et al. 2003; Giavalisco et al. 2004). In particular, the deep *Spitzer* MIPS observations at 24 μm (Chary et al., in prep.) and 70 μm (Frayer et al., in prep.) are important to probe re-emission by dust at rest-frame mid-IR wavelengths. This analysis is also based on the available broad-band photometry from the UV to the near-IR (Kurk et al., in prep.), since it utilises galaxy parameters derived from model fits to the photometric data. For instance, both the star-formation rate (SFR) and the total stellar mass ($M_\star$) of a galaxy used here were derived from fitting broad-band SEDs (extending from *U* band to the IRAC 8 μm band) using the *Hyperz* code of Bolzonella et al. (2000), the redshift being fixed to the measured spectroscopic value (cf. Pozzetti et al., in prep.). In particular, fitting made use of the stellar population synthesis models of Maraston (2005)[1] including a Salpeter (1955) initial mass function (IMF) and fixed solar metallicity ($Z_\odot$), whereas age was allowed to vary up to the lookback time of the object. Star-formation histories (SFHs) were described by exponentials with *e*-folding times between 100 Myr and infinity (constant SFR). Dust attenuation was assumed to be described as in Calzetti et al. (2000).

Finally, we note that morphologies of the GMASS galaxies were determined by a *Galfit* (Peng et al. 2002) analysis of the HST-ACS imaging at 8500 Å from the GOODS-S (Cassata et al., in prep.). For $1.5 < z < 2.5$, the *z*-band maps rest-frame mid-UV to near-UV wavelengths, so that the morphological parameters

[1] We use these particular models because they are the only published models including the thermally pulsating asymptotic giant branch phase for intermediate-mass (2−5 $M_\odot$) stars.

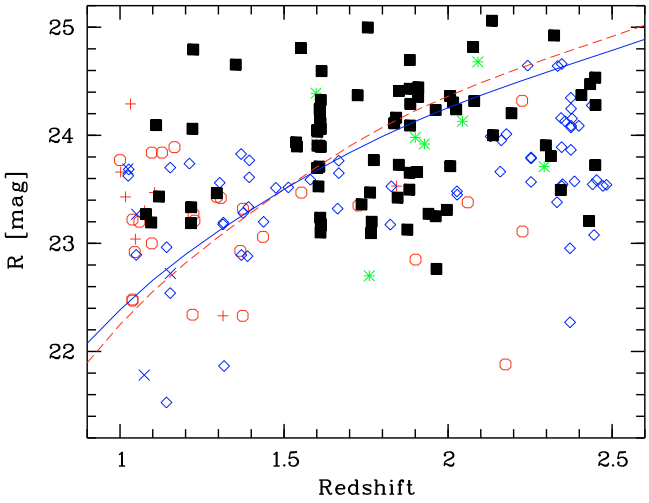

Fig. 1. R-band magnitude versus redshift for the total sample of 186 actively star-forming galaxies at $1 < z < 2.5$ selected from the GMASS (filled squares), FDF spectroscopic survey (lozenges and crosses), the K20 survey (circles and plus signs), and the GDDS (asterisks). Crosses, plus signs, and asterisks mark galaxies without a determination of the UV continuum slope. To illustrate selection biases, the curves show lines of constant luminosity for typical $1 < z < 1.5$ FDF (solid line) and K20 (dashed line) spectra. Both curves intersect at $R = 23.5$ and $z = 1.5$.

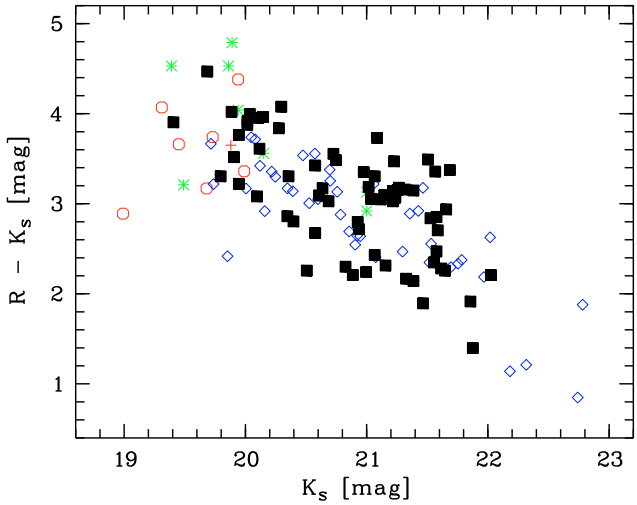

Fig. 2. $R - K_s$ colour versus K_s magnitude for sample galaxies with $1.5 < z < 2.5$. Symbols are the same as in Fig. 1.

reflect the distribution of young stellar populations. In this study, we adopt measurements of the effective radius r_e, the Sérsic (1968) index n_{ser}, and the axial ratio b/a. Moreover, we investigate the CAS parameters concentration C and asymmetry A measured according to a method described by Cassata et al. (2005).

2.2. The FDF, K20, and GDDS samples

The GMASS sample is complemented by the spectroscopic sample investigated by NPPS, consisting of 108 actively star-forming galaxies at $1 < z < 2.5$. Of these 108 objects, 66 galaxies were selected from the (mostly) I-limited spectroscopic catalogue of the FORS deep field (FDF) spectroscopic survey (Noll et al. 2004) and originally inspected for $z > 2$ by NP05. In addition, 34 galaxies were taken from the $K_s < 20$-selected K20 survey in the GOODS-S and a field around quasar 0055-2659 (Cimatti et al. 2002; Mignoli et al. 2005), and 8 galaxies were selected from the I- and K_s-limited Gemini deep deep survey (GDDS, Abraham et al. 2004). For 88 objects from the FDF and K20 samples, the UV continuum slope could be determined in addition to the presence/absence of the UV bump (see NPPS).

2.3. Basic sample properties

Figure 1 shows the range of R-band magnitudes and redshifts covered by the different samples considered in this study, including the 10 GMASS UV-luminous galaxies at $1 < z < 1.5$. All but two NPPS objects are brighter than $R = 24$ for $z < 2$, and a few reach $R = 24.7$ at higher redshifts. With GMASS, fainter galaxies ($24 < R < 25$) represent half of the sample ($\langle R \rangle = 23.9$) and are probed for the entire redshift range studied. Additional differences in the redshift distributions exist, as previously anticipated: 76% of the K20 galaxies are at $1 < z < 1.5$, whereas the FDF sample mainly consists of objects at $1 < z < 1.5$ (38%) or $2 < z < 2.5$ (52%); in contrast, 67% of the GMASS objects are located at $1.6 < z < 2.1$. As indicated by curves of fixed luminosity in Fig. 1, the brightness requirements for spectroscopy (and possible evolution in the galaxy population) cause an unavoidable increase in the average rest-frame UV luminosity of the sample with redshift. Therefore, redshift-dependent results have to be interpreted with care.

As additional information, Fig. 2 illustrates the $R - K_s$–K_s colour–magnitude diagram of the sample galaxies at $1.5 < z < 2.5$, where most of the selected GMASS galaxies lie. There is good overlap between GMASS and NPPS objects at these redshifts, the GMASS galaxies being only 0.2 mag brighter and 0.3 mag redder than the coeval FDF galaxies ($K_s = 20.8$ versus 21.0, and $R - K_s = 3.1$ versus 2.8, respectively). Hence, in spite of the different selection criteria (i.e., based on the rest-frame near-IR and UV domains for the GMASS and FDF samples, respectively), the photometric properties of the selected GMASS galaxies are similar to those of the selected NPPS galaxies. As Fig. 2 demonstrates, no extremely red object (e.g., Pozzetti & Mannucci 2000) is present in the full sample (cf. Fig. 2). Aspects of dust attenuation in these objects were discussed by Pierini et al. (2004a) and Pierini et al. (2005). From the results of these analyses, we conclude that our sample galaxies are probably neither heavily reddened, young starbursts nor normal star-forming, bulge-dominated systems. In principle, the lack of faint red galaxies in our sample due to brightness limits could affect the results of our analysis. However, investigations of the relation between mass and extinction (Greggio et al. 2008) suggest that relatively massive star-forming galaxies with such properties could be rare by nature. Hence, we can reasonably assume that not detecting such galaxies (if any) does not bias our conclusions.

3. Data analysis

In this section, we briefly describe our method for constraining the shape of the UV extinction curve from optical spectroscopy of high-redshift galaxies. In a first step, constraints are obtained from a suitable parametric description of the rest-frame UV SED of a galaxy (Sect. 3.1), as extensively discussed in NP05 and NPPS. In a second, new step, the detailed shape of the observed UV bump is derived by fitting a model (Sect. 3.2).

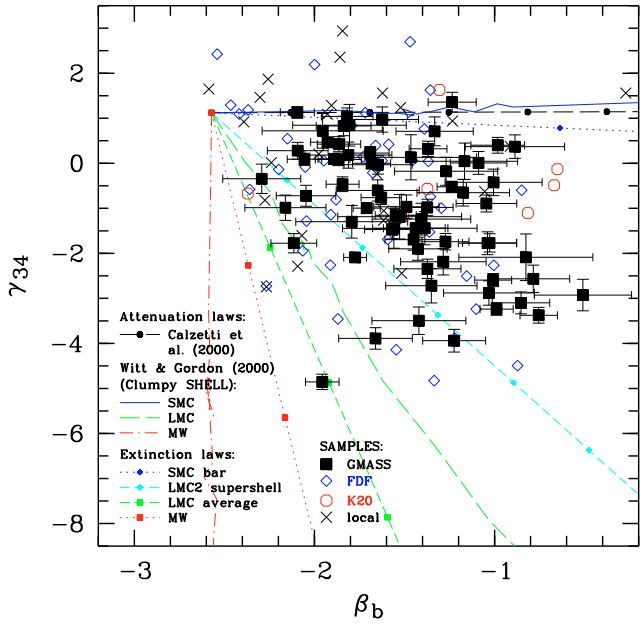

Fig. 3. The UV-bump indicator γ_{34} versus the UV reddening measure β_b for the GMASS (filled squares), FDF (open lozenges), and K20 galaxies (open circles) at $1.5 < z < 2.5$, and a comparison sample of 24 local starburst galaxies (crosses; see NP05). The diagram also shows different dust attenuation models (see legend) for a Maraston (2005) model with Salpeter IMF, continuous SF, an age of 100 Myr, and solar metallicity. The symbols are plotted in intervals of $\Delta E_{B-V} = 0.1$. A Maraston model with a SF e-folding time of 3 Gyr and an age of 3 Gyr would produce intrinsically redder continua and, thus, would slightly shift the plotted model curves by 0.20 to the right and by 0.08 to the top.

3.1. Parametric description of the UV continuum

NP05 introduced a parametrisation of the rest-frame UV SED of a star-forming, dusty galaxy, which highlights the presence of the UV bump, and offers constraints on the far-UV slope of the extinction curve. It is based on power-law fits to different subregions of the UV continuum, in a similar way to the parametrisation used by Calzetti et al. (1994) for measuring the UV continuum slope β. Hereafter, we utilise only the parameters γ_{34} and β_b (introduced by NPPS). The first parameter represents the difference between the power-law slopes γ_3 and γ_4 measured in the wavelength ranges 1900–2175 Å and 2175–2500 Å, respectively, excluding strong narrow features. By construction, γ_{34} is particularly suitable for identifying the presence of the broad absorption feature centred on about 2175 Å: the more negative γ_{34}, the higher is the probability that a UV bump of some strength is present (see Fig. 3). Moreover, γ_{34} depends only very little on stellar population properties (NP05). Negative values of γ_{34} are almost impossible for combinations of stellar populations attenuated by bump-less reddening laws only. NP05 chose $\gamma_{34} = -2$ as a fiducial threshold for a robust detection of the UV bump (see NPPS for an updated discussion of this threshold). The second parameter β_b, measured at 1750–2600 Å, indicates the continuum slope across the UV bump, and is therefore a reasonable proxy for the dust reddening of the UV continuum, as well as β (cf. NPPS). As in NPPS, β_b is preferred to β (measured down to Lyα) because the latter cannot be derived from optical spectra for galaxies at $z < 2$. By using β_b for all galaxies across the entire redshift range 1.0–2.5, we are able to compare their properties in a consistent way.

We know that γ_{34} alone does not infer whether the extinction curve is similar to either the MW or LMC curve, because it indicates the *apparent* amplitude/area of the UV bump, which is a function of the dust opacity (see, e.g., Witt & Gordon 2000). Since the dust reddening of UV SEDs depends on the opacity as well, it is the distribution of a galaxy in the β_b–γ_{34} plane that identifies the extinction curve (see Fig. 3).

3.2. Lorentzian-like fitting of the UV bump

The parameter γ_{34} can easily be measured in spectra with a relatively narrow spectral coverage, and even in noisy ones, but it loosely constrains the observed shape of the UV bump, and, thus, the kind of extinction curve (i.e., MW-, LMC-, or SMC-like). The high S/N and wavelength coverage of the GMASS spectra offer the opportunity for a more accurate description of the UV bump. In particular, for $z \sim 2$ the UV bump sits almost in the middle of the observed wavelength range, which allows the bump to be fitted in its shallowest wings. For optimum results, we investigate stacked spectra (introducing subsampling) and not individual ones (see Sect. 4.2).

According to Fitzpatrick & Massa (1990, FM), the shape of the UV bump present in extinction curves is most accurately described by a Lorentzian-like "Drude" profile

$$D(x, x_0, \gamma) = \frac{x^2}{(x^2 - x_0^2)^2 + x^2\gamma^2}, \quad (1)$$

where x, x_0, and γ are expressed in units of inverse wavelength, x_0 being the central wavelength and γ the inverse of the *FWHM* of the UV bump. In the FM parametrisation, extinction curves $k(\lambda-V)$ are normalised by the reddening E_{B-V}, and the UV bump is reproduced by $c_3\, D(x, x_0, \gamma)$, where c_3 is an amplitude (in units of inverse wavelength in quadrature). In later work, Fitzpatrick & Massa (2007) defined two additional parameters, based on combinations of the basic parameters x_0, γ, and c_3. In particular, $E_{\rm bump} \equiv c_3/\gamma^2$ is the maximum height above the linear baseline extinction, and $A_{\rm bump} \equiv \pi c_3/(2\gamma)$ indicates the area subtended by the UV bump.

In analogy with the FM formalism, we characterise the observed UV-bump in galaxy spectra as an excess with respect to a baseline attenuation. At variance with extinction curves measured for sightlines to individual stars, the observed UV bump in a galaxy spectrum is affected by radiative transfer effects since spectra probe large regions of galaxies (see, e.g., Ferrara et al. 1999; Pierini et al. 2004b, in case of photometry). We set the baseline to be the attenuation curve of nearby starburst galaxies (Calzetti et al. 2000), where the wavelength dependence is fixed and the amount of attenuation at a given wavelength scales with the *observed* reddening E_{B-V} at optical wavelengths. Since the curvature of the selected reference curve for the continuum attenuation is not supposed to differ strongly from the unknown real shape within the range of the UV bump, the choice of the baseline mostly affects the measured amplitudes of the UV bump, while centre and width are expected to be almost invariable. Our approach is unorthodox but allows us to link our results to those obtained from studies of galaxy evolution, which adopt the Calzetti law as a description of dust attenuation in galaxies at cosmological distances. Therefore, we refer to the parameters derived for our sample galaxies as "FM-like".

In our procedure, regions of the spectra that exclude the 2175 Å feature[2] and other known strong spectral lines are fitted

[2] A region across the UV bump of width 900–1000 Å is masked to avoid even faint wings.

by different Maraston (2005) models with exponentially decaying star-formation rates and reddened by a Calzetti et al. (2000) attenuation law. By doing so, we are able to interpolate across the UV bump. Taking into account uncertainties and approximations, fits are considered to be "good" if their significance reaches at least 95% of that of the best-fit model. For these good fits, the residual 2175 Å feature (if any) is detectable in a spectrum created by obtaining the ratio of the initial spectrum to the model. Retrieving the properties of the observed UV bump therefore depends only on the best-fit E_{B-V} value of the Calzetti law. The uncertainty in E_{B-V} mainly affects the observed UV-bump amplitude c_3, whereas x_0 and γ are less dependent on the best-fit model. These FM-like parameters are derived from Lorentzian fits to each continuum-subtracted UV bump. Lorentzian fits are considered as "good" if their significance is at least 95% of that of the best-fit model. They are used to compute the mean and standard deviation of each FM-like parameter. To estimate the influence of noise on these fits, a set of synthetic spectra modified on the basis of the error function are computed and analysed in the same way as the real data. The final variance in the FM-like parameters measured for a stacked spectrum is given by the standard deviation of the good fits and the statistical noise, added in quadrature.

4. Results

We first present and discuss results obtained from the parametrisation and modelling of the rest-frame UV continua of our high-redshift galaxies (Sect. 4.1), whereas detailed shapes of the observed UV bumps are illustrated in Sect. 4.2. The link between carriers of the UV bump and properties of the parent galaxies is addressed in Sect. 4.3. Finally, the existence of a relation between the presence of these carriers and the amount of re-emission by dust at rest-frame 8 μm is discussed in Sect. 4.4.

4.1. Extinction curves with a UV bump are not unusual among high-redshift galaxies with gas and dust

Figure 4 illustrates the redshift distribution of the proxy for the presence of a UV bump in spectra, γ_{34}, and the continuum slope in the UV-bump region, β_b, for the GMASS, FDF, K20, and GDDS samples. A total of 186 actively star-forming, intermediate-mass galaxies at $1 < z < 2.5$ is shown, including the 10 GMASS objects at $1 < z < 1.5$. As from NPPS, the fraction of UV-luminous galaxies at these redshifts that clearly exhibit a 2175 Å feature in their spectra (i.e., $\gamma_{34} < -2$) is about 30%. In particular, this fraction is 25% for the combined FDF and K20 samples at $1 < z < 1.5$, and 36% for the FDF sample at $2.2 < z < 2.5$. A similar fraction of 24% *s*ignificant *U*V *b*ump *g*alaxies (SUBGs) characterises the GMASS sample at $1.5 < z < 2.5$, 13 out of 17 detections being for objects at $1.5 < z < 2.2$. This fraction drops to 10% for the GMASS galaxies at $1 < z < 1.5$.

We verified that, for the GMASS sample (see Sect. 2), subsampling in terms of rest-frame UV luminosity (i.e., splitting the sample at $R = 24.0$) or large scale structure (see the overdensity of galaxies at $z \sim 1.61$; Kurk et al. 2008b) does not impact this fraction. Hence, we conclude that the non-detection of SUBGs at $1.5 < z < 2.5$ in the FDF and K20 samples (see NPPS) is probably due to low number statistics, plus possible selection and detection biases. In support of this conclusion, we note that the distributions of the GMASS, FDF, and K20 galaxies at $1.5 < z < 2.5$ in the β_b–γ_{34} diagnostic diagram are similar (Fig. 3). In particular, the average value of γ_{34} for the GMASS galaxies at $1.5 < z < 2.5$ is consistent with that of coeval FDF galaxies (-1.01 ± 0.17 versus -0.70 ± 0.30) within the errors. The average value of the reddening in the UV, β_b, is slightly higher (-1.48 ± 0.05 versus -1.71 ± 0.07). At $1 < z < 1.5$, the combined FDF and K20 samples

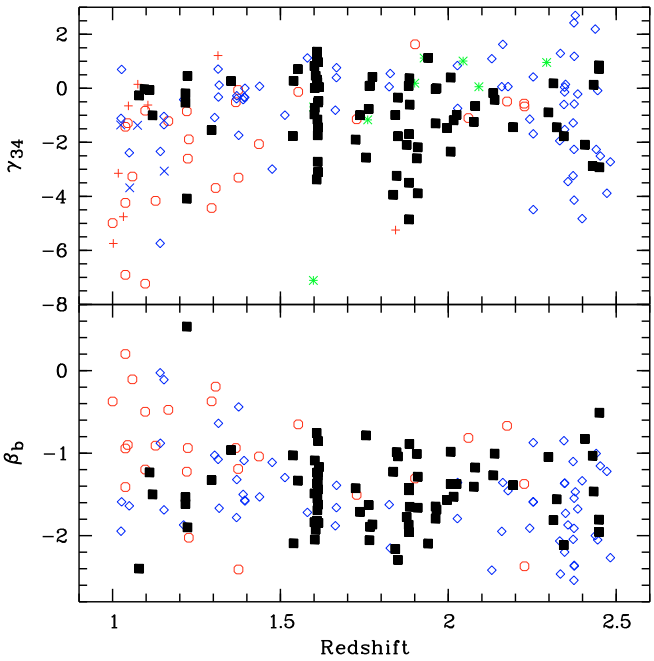

Fig. 4. The UV-bump indicator γ_{34} (*upper panel*) and the UV reddening measure β_b (*lower panel*) versus redshift for 78 GMASS galaxies at $1 < z < 2.5$ (filled squares) in comparison to 108 galaxies from NPPS (20 without β_b measurement). Symbols are the same as in Fig. 1.

Table 1. Average properties of the three GMASS subsamples at $1.5 < z < 2.5$

Par.	$\gamma_{34} > -2$ $\beta_b < -1.5$	$\gamma_{34} > -2$ $\beta_b > -1.5$	$\gamma_{34} < -2$
N	29	23	16
z	1.86 ± 0.05	1.85 ± 0.05	1.91 ± 0.06
R	23.74 ± 0.09	24.20 ± 0.10	23.99 ± 0.13
K_s	21.09 ± 0.11	20.74 ± 0.15	20.60 ± 0.13
γ_{34}	-0.20 ± 0.16	-0.62 ± 0.19	-3.02 ± 0.19
β_b	-1.83 ± 0.04	-1.24 ± 0.04	-1.18 ± 0.10
$\log L_{1500}$ [W/Å]	33.95 ± 0.04	33.68 ± 0.03	33.82 ± 0.07
$\log L_{2500}$ [W/Å]	33.61 ± 0.04	33.46 ± 0.04	33.60 ± 0.06
E_{B-V}	0.133 ± 0.020	0.244 ± 0.022	0.304 ± 0.020
$\log L_{bol}$ [$L_\odot$]	11.37 ± 0.08	11.56 ± 0.07	11.85 ± 0.04
$\log SFR$ [$M_\odot$/yr]	1.53 ± 0.09	1.70 ± 0.08	2.05 ± 0.04
$\log M_\star$ [$M_\odot$]	9.94 ± 0.05	10.12 ± 0.08	10.15 ± 0.07
$\log \phi$ [Gyr^{-1}]	0.52 ± 0.08	0.51 ± 0.11	0.85 ± 0.07
r_e [kpc][a]	2.84 ± 0.48	2.65 ± 0.37	2.52 ± 0.38
n_{ser}	1.56 ± 0.32	1.79 ± 0.44	0.77 ± 0.15
b/a	0.46 ± 0.03	0.54 ± 0.04	0.46 ± 0.04
C_{CAS}	2.57 ± 0.07	2.63 ± 0.07	2.55 ± 0.08
A_{CAS}	0.40 ± 0.03	0.42 ± 0.03	0.43 ± 0.03
$f_{24\,\mu m}$ [μJy]	37.3 ± 14.8	39.1 ± 10.4	63.3 ± 9.9
$\log L_{8\,\mu m}$ [$L_\odot$]	10.28 ± 0.07	10.35 ± 0.09	10.73 ± 0.07
$\log L_{IR}$ [$L_\odot$]	11.11 ± 0.09	11.21 ± 0.11	11.66 ± 0.08
$\log(L_{IR}/L_{UV})$	0.50 ± 0.10	0.89 ± 0.13	1.25 ± 0.12

[a] From $\log r_e$.

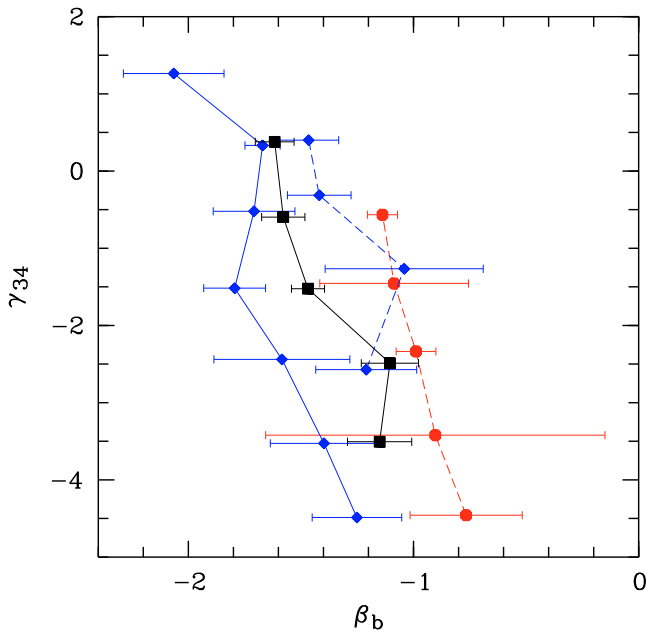

Fig. 5. Average UV reddening measure β_b for unit bins of the UV-bump indicator γ_{34}. The following subsamples are shown: GMASS for $1.5 < z < 2.5$ (squares and solid lines), FDF for $1.5 < z < 2.5$ (lozenges and solid lines), FDF for $1 < z < 1.5$ (lozenges and dashed lines), and K20 for $1 < z < 1.5$ (circles and dashed lines). Only bins with at least two data points are plotted. The β_b uncertainties shown are mean errors derived from the sample variance and the uncertainties of individual measurements.

exhibit stronger 2175 Å features ($\langle\gamma_{34}\rangle = -1.23 \pm 0.23$) and redder UV continua ($\langle\beta_b\rangle = -1.23 \pm 0.08$) due to a population of galaxies with extreme UV-continuum properties, which is not present in our sample at higher redshifts (see Fig. 4).

The GMASS sample confirms that more negative values of γ_{34} are found as β_b increases. The galaxy distribution in Fig. 3 is interpreted by making use of different dust-reddened stellar-population models. In particular, for a 100 Myr-old, solar metallicity, continuous star-formation model of Maraston (2005), we show models with increasing E_{B-V} for the attenuation law of Calzetti et al. (2000), different clumpy shell models of Witt & Gordon (2000), and uniform screen models using different extinction curves obtained for the SMC, LMC (Gordon et al. 2003), and the MW (Cardelli et al. 1989). The distribution of the data points is well constrained by these models, and evidence of extinction curves with a form other than that of the SMC (with no UV bump) is clear. The evidence of non-SMC extinction curves is insensitive to the choice of the stellar-population model. For instance, considering a Maraston model with a SFR e-folding time of 3 Gyr at an epoch of 3 Gyr after the beginning of the SF activity would shift the plotted model curves only by +0.20 in β_b and +0.08 in γ_{34}.

According to the models shown in Fig. 3, the presence of a moderate UV bump (as in the LMC extinction curve) is suggested. However, the identification of the extinction curve becomes complex, if models implementing age-dependent extinction scenarios are considered. In fact, as a given simple stellar population becomes less attenuated as time goes by (i.e., as the average age of the stars increases), extinction curves with more pronounced UV bumps (e.g., as for the MW) are allowed by the distribution of the data points (see NPPS for a detailed discussion). This scenario can be implemented by, e.g., realistic dust/star distributions similar to those of nearby disc galaxies (e.g., Silva et al. 1998; Pierini et al. 2004b). However, it cannot explain the existence of spectra with extremely negative values of γ_{34}. In this case, extraplanar dust must be invoked (NPPS). Hence, time-independent screen models (without scattering) or dusty shells appear to describe dust attenuation well in the high-redshift galaxies of our sample, and, thus, the data distribution in Fig. 3.

Besides the overall agreement, some slight but interesting differences between samples exist, as suggested by Fig. 5, which reproduces average values of β_b for $\Delta\gamma_{34} = 1$ bins. In fact, moving from the FDF galaxies at $1.5 < z < 2.5$ ($\langle z\rangle = 2.21$) to the GMASS galaxies in the same redshift range ($\langle z\rangle = 1.89$), and, then, from the FDF galaxies at $1 < z < 1.5$ ($\langle z\rangle = 1.27$) to the K20 galaxies in the same redshift range ($\langle z\rangle = 1.18$), β_b tends to increase or the rest-frame UV continua become redder. Comparison of values obtained for the different samples shows that the significance of this trend ranges between 1 and 3σ. The most reliable values are found for the largest redshift differences. In principle, differences in the selection criteria, average luminosities, and redshifts (partly driven by the small number statistics available for individual samples) or systematic errors[3] could play a role. For the GMASS galaxies at $1.5 < z < 2.5$, we checked that the variation in β_b is negligible (0.06 ± 0.09) for objects brighter or fainter than $R = 24$. Therefore, the presence of redder UV continua as redshift decreases may have a physical origin, i.e., ageing of the overall stellar population and/or an increase in the overall ISM opacity. A change in the dust composition and/or distribution is possible as well.

Interestingly, the sample of 24 local starburst galaxies observed by IUE and selected by NP05 exhibits relatively bluer UV continua than our sample galaxies: $\langle\beta_b\rangle = -1.79 \pm 0.11$ for $\langle\gamma_{34}\rangle = 0.27 \pm 0.32$. Suitable models of a MW-like galaxy that involve stellar population synthesis and radiative transfer for a disc geometry (see Pierini et al. 2003) predict redder UV continua than starbursts in the local Universe. According to the models used by NP05, ageing of the stellar populations would however produce only a moderate shift in β_b equal to 0.1–0.2. Unfortunately, a robust age-dating of the stellar populations of all our sample galaxies is not possible, since the redshifted Balmer and 4000 Å breaks are detectable in optical spectra only for $z < 1.5$ (see NPPS), and model fitting provides quite uncertain age estimates.

4.2. Constraining the attenuation curve

In analogy with NP05 and NPPS[4], we divide the GMASS sample of galaxies at $1.5 < z < 2.5$ into subsamples, using the same thresholds of $\beta_b = -1.5$ and $\gamma_{34} = -2$. In particular, we consider one GMASS subsample with $\gamma_{34} < -2$, and two with $\gamma_{34} > -2$ that differ in terms of β_b. For $1.5 < z < 2.5$, 16 GMASS galaxies are SUBGs, whereas 23 and 29 GMASS galaxies have $\gamma_{34} > -2$ plus red or blue UV continua, respectively. Average values of γ_{34} and β_b are listed in Table 1 for these GMASS subsamples.

Figure 6 shows a comparison of the composite spectra of the GMASS galaxies at $1.5 < z < 2.5$ exhibiting either weak evidence (at most) of a broad absorption feature centred on 2175 Å

[3] The FDF galaxies dominate the sample of galaxies beyond $z = 2.3$. Their measured values of β_b can be affected by systematic errors due to the presence of strong OH residuals in the red optical wavelength region, where the redshifted β_b was measured.

[4] The NPPS sample of galaxies at $1 < z < 1.5$ is divided into a blue ($\beta_b < -1.5$) and two red subsamples differing in γ_{34}.

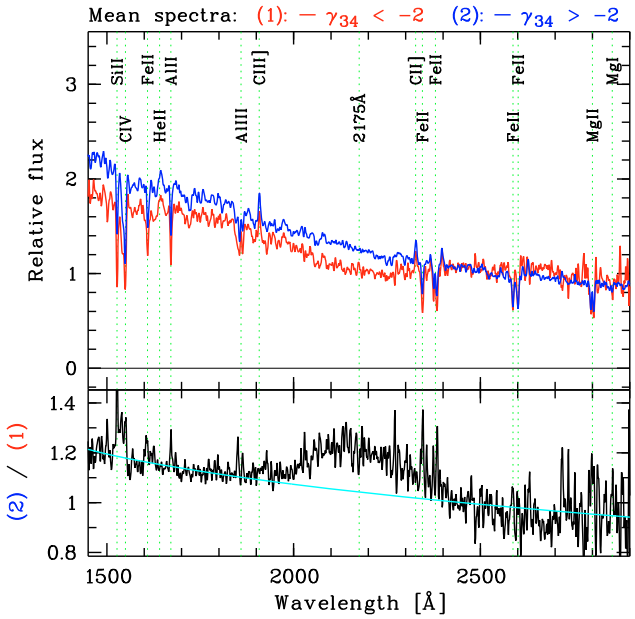

Fig. 6. Comparison of composite spectra of $1.5 < z < 2.5$ GMASS galaxies with $\gamma_{34} > -2$ (blue) and $\gamma_{34} < -2$ (red), respectively. The lower panel gives the ratio of both composites, normalised at 2400−2570 Å. Deviations from a Calzetti law in the UV-bump range are illustrated by the overplotted best-fit Calzetti attenuation curve with $E_{B-V} = 0.08$.

in their spectra ($\gamma_{34} > -2$), or a secure one ($\gamma_{34} < -2$). The presence of this feature in the second (more reddened) composite spectrum is evident by eye.

4.2.1. The shape of the UV bump

Lorentzian-like fits are applied to the stacked rest-frame UV continua obtained from galaxies at $1.5 < z < 2.5$ in the three GMASS subsamples, and from FDF and K20 galaxies at $1.0 < z < 1.5$ with $\gamma_{34} < -2$[5], as described in Sect. 4.1. The resulting FM-like parameters describing the morphology of the observed UV bump – i.e., centre x_0 (or λ_0), γ, and amplitude c_3 – and their errors are listed in Table 2, with the maximum height $E_{\rm bump}$ and area $A_{\rm bump}$ of the observed UV bump, and the mean E_{B-V} of the best-fit Calzetti et al. (2000) attenuation law used as a baseline. We note that the values of E_{B-V} obtained from this Lorentzian-like fitting are consistent with those obtained from the SED fitting of GMASS galaxies (see Sect. 2.1) within the errors. However, we acknowledge that differences in E_{B-V} become higher for red galaxies with some signature of the UV bump in their spectra.

Figure 7 shows the quality of the Lorentzian-like best-fit functions of the observed (residual) UV bumps obtained for the four subsamples. We note that radiative transfer effects only smooth out the UV bump in disc configurations (cf. Ferrara et al. 1999; Pierini et al. 2004b). Furthermore, no significant variation in the width of the observed UV bump is found for the different radiative transfer models of Witt & Gordon (2000) for a given dust composition. Thus, we can assume that the residual UV bumps determined from the composite spectra of our galaxies are closely related to those present in the extinction curve

[5] Their composite spectrum is cut at 1800 Å, since only a few spectra extend shortwards. Possible effects of the UV bump on the 1800–1900 Å region have been considered.

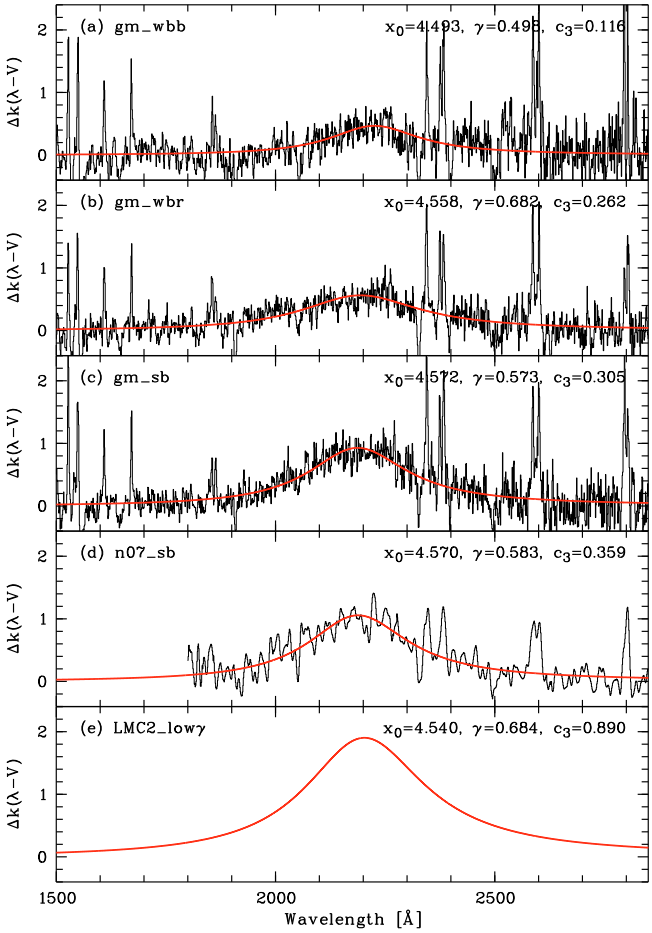

Fig. 7. Best Lorentzian fits of the bump component of the average extinction curves of the three GMASS subsamples at $1.5 < z < 2.5$ **(a–c)** and a subsample of FDF and K20 galaxies at $1.0 < z < 1.5$ with $\gamma_{34} < -2$ **(d)**. Moreover, the average 2175 Å bump of a sample of measurements in the LMC 2 supershell region close to 30 Dor showing low γ is presented **(e)**. More details about the samples and the fits can be found in Table 2.

characterising their dust. As a first result, Fig. 8 indicates a comfortably good correlation between the maximum height of the UV bump $E_{\rm bump}$ (dependent on the *FWHM* and amplitude) and the independently measured γ_{34}. Since the increase in E_{B-V} with decreasing γ_{34} in our sample (see Table 2) is obviously unable to remove this correlation, the increasingly negative values of γ_{34} are indeed associated with more pronounced UV bumps.

The central wavelengths and widths of the residual UV bumps obtained for GMASS SUBGs at $1.5 < z < 2.5$ and FDF and K20 SUBGs at $1.0 < z < 1.5$ are almost identical. They have counterparts among those measured along different sightlines towards the MW and LMC[6] (see Fig. 9). In particular, the most suitable local counterpart is the supershell region LMC 2 close to 30 Dor, for which the average UV bump from different sightlines (excluding two outliers) is centred on 2203 ± 26 Å and has a *FWHM* equal to 332 ± 21 Å (cf. Gordon et al. 2003). For instance, the central wavelength and *FWHM* of the residual UV bump obtained for the composite spectrum of GMASS SUBGs

[6] The average values of the FM parameters for the MW (Fitzpatrick & Massa 2007) and LMC (Gordon et al. 2003) are: 2180 Å (central wavelength), 440 Å (*FWHM*) or 0.93 μm^{-1} (γ), and 3.0 or 2.7 (c_3), respectively.

Table 2. UV-bump parameters analogous to those introduced by Fitzpatrick & Massa (1990).

Sample[a]	Selection	E_{B-V}	x_0 [μm^{-1}]	λ_0 [Å]	γ [μm^{-1}]	*FWHM* [Å]
(a) gm_wbb	GMASS, $1.5 < z < 2.5$, $\gamma_{34} > -2, \beta_b < -1.5$	0.164 ± 0.069	4.493 ± 0.024	2226 ± 12	0.498 ± 0.113	247 ± 56
(b) gm_wbr	GMASS, $1.5 < z < 2.5$, $\gamma_{34} > -2, \beta_b > -1.5$	0.286 ± 0.071	4.558 ± 0.024	2194 ± 11	0.682 ± 0.052	328 ± 25
(c) gm_sb	GMASS, $1.5 < z < 2.5$, $\gamma_{34} < -2$	0.296 ± 0.069	4.572 ± 0.010	2187 ± 05	0.573 ± 0.021	274 ± 10
(d) n07_sb	FDF/K20, $1.0 < z < 1.5$, $\gamma_{34} < -2$	0.344 ± 0.078	4.570 ± 0.019	2188 ± 09	0.583 ± 0.083	279 ± 38
(e) LMC2_lowγ	LMC 2 supershell ($\gamma < 1$)	0.188 ± 0.009	4.540 ± 0.053	2203 ± 26	0.684 ± 0.042	332 ± 21
Sample[a]	Selection	c_3 [μm^{-2}]	$E_{\rm bump}$	$A_{\rm bump}$ [μm^{-1}]		
(a) gm_wbb	GMASS, $1.5 < z < 2.5$, $\gamma_{34} > -2, \beta_b < -1.5$	0.116 ± 0.055	0.467 ± 0.267	0.366 ± 0.192		
(b) gm_wbr	GMASS, $1.5 < z < 2.5$, $\gamma_{34} > -2, \beta_b > -1.5$	0.262 ± 0.040	0.562 ± 0.106	0.602 ± 0.104		
(c) gm_sb	GMASS, $1.5 < z < 2.5$, $\gamma_{34} < -2$	0.305 ± 0.020	0.928 ± 0.077	0.835 ± 0.062		
(d) n07_sb	FDF/K20, $1.0 < z < 1.5$, $\gamma_{34} < -2$	0.359 ± 0.121	1.056 ± 0.186	0.968 ± 0.251		
(e) LMC2_lowγ	LMC 2 supershell ($\gamma < 1$)	0.890 ± 0.128	1.903 ± 0.320	2.044 ± 0.320		

[a] For the samples at high redshift, the given errors are based on the uncertainties in the continuum of the mean spectrum without the 2175 Å feature, E_{B-V}, and the FM-like parameter fit. For the LMC, they represent the sample variance.

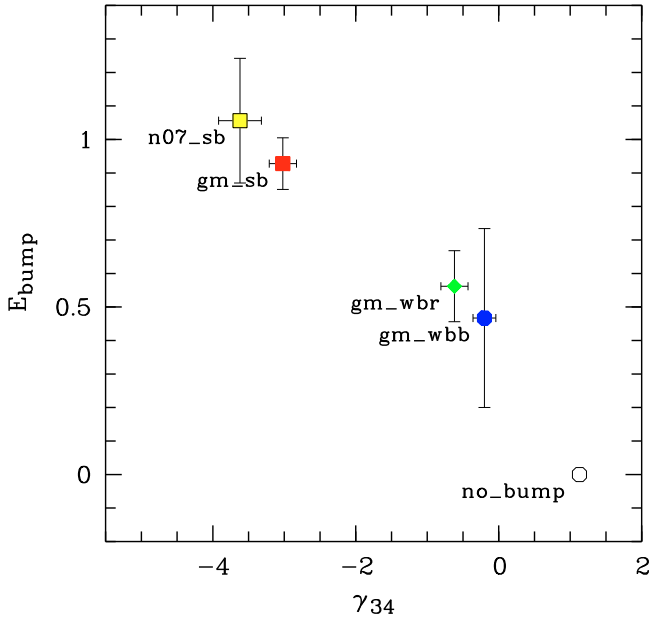

Fig. 8. Amplitude of the UV bump in the extinction curve $E_{\rm bump}$ (see Sect. 3.2) versus γ_{34} indicating the strength of the 2175 Å feature in the spectrum for the three subsamples of GMASS galaxies at $1.5 < z < 2.5$ and the NPPS subsample of $1 < z < 1.5$ galaxies with γ_{34}. Labels are the same as in Fig. 7 and Table 2 but for an open circle, which marks the position of an extinction curve without any UV bump. The corresponding γ_{34} is given for the stellar population parameters described in Fig. 3.

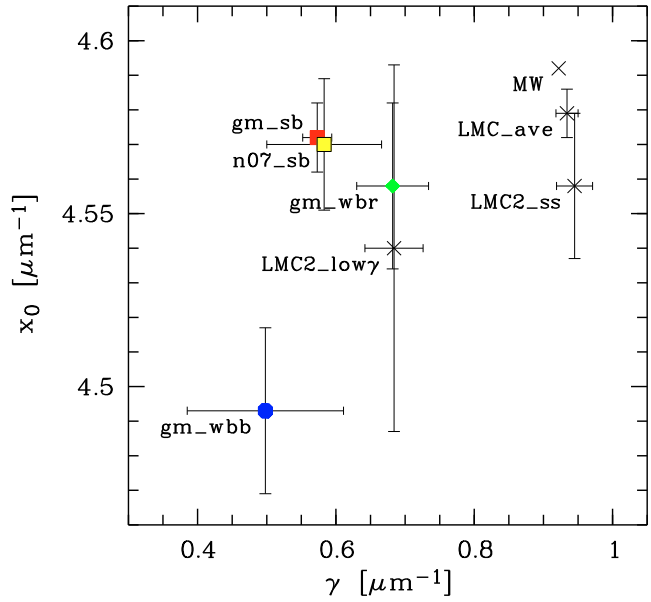

Fig. 9. FM-like parameters x_0 (the inverse central wavelenth of the UV bump) and γ (linked to the inverse *FWHM* of the UV bump) for the three subsamples of GMASS galaxies at $1.5 < z < 2.5$ and the NPPS subsample of $1 < z < 1.5$ galaxies with $\gamma_{34} < -2$ (filled symbols). Labels are the same as in Fig. 7 and Table 2. Moreover, crosses mark average FM parameters for the Milky Way (Fitzpatrick & Massa 2007) and different LMC environments (Gordon et al. 2003). The latter are the average LMC ("LMC_ave"), the entire LMC 2 supershell region ("LMC2_ss"), and the LMC 2 supershell region restricted to stars with $\gamma < 1\,\mu$m^{-1} ("LMC2_lowγ"). The errors given are measurement uncertainties of the FM parameters for the corresponding mean extinction curves except for "LMC2_lowγ", for which sample mean errors are provided.

are equal to 2187 ± 5 Å and 274 ± 10 Å, respectively. In general, the observed UV bumps of our high-redshift galaxies are relatively narrow, since they exhibit only about 60% of the typical widths measured for sightlines towards the MW and LMC.

In addition, we note that the two composite spectra obtained for either the blue or red GMASS galaxies at $1.5 < z < 2.5$ with no strong evidence of a UV bump in their individual spectra (i.e., with $\gamma_{34} > -2$) nevertheless exhibit a weak one. In either case, the central wavelength and width of the residual UV bump are not dissimilar to those obtained for galaxies with $\gamma_{34} < -2$. This tells us that some traceable dust similar to that in the supershell region LMC 2 seems to be present also in a non-negligible fraction of the blue and red GMASS non-SUBGs at $1.5 < z < 2.5$.

4.2.2. The shape of the attenuation curve

Our previous results imply that, at least for part of the high-redshift galaxy population, the functional form of the attenuation curve differs significantly from a Calzetti law. This is demonstrated by Fig. 6, which shows the best-fit Calzetti law for the ratio of the composite spectrum for $\gamma_{34} > -2$ to that for $\gamma_{34} < -2$. Neglecting possible differences in the age distribution of the stellar populations of both composite spectra, the resulting spectrum in the lower panel of Fig. 6 should reflect only a difference in reddening, if the Calzetti law holds universally. As expected,

the best-fit Calzetti law with $E_{B-V} = 0.08$ fails to reproduce the UV bump region. However, the reliable wavelength range of the composites (from 1450 to 2900 Å) is too narrow to allow a significant deviation in the slope of the attenuation law to be detected. Moreover, this simple test does not provide any constraints on the reliability of the wavelength-dependent amount of attenuation predicted by the Calzetti law. Investigating the shape of the attenuation curve across a wide wavelength range would require a thorough study of a much larger data set and probably more sophisticated modelling. This is beyond the scope of the present work and is deferred to a future paper.

For now, we propose to modify the Calzetti et al. (2000) law $k(\lambda)$ by adding a Lorentzian-like UV bump $c_3 D_{x_0,\gamma}(\lambda)$ (see Eq. (1) in Sect. 3.2) and derive the wavelength-dependent attenuation in magnitudes by

$$A(\lambda) = E_{B-V}\,(k(\lambda) + c_3 D_{x_0,\gamma}(\lambda)). \quad (2)$$

Since we have already used the Calzetti law as a baseline for the derivation of the FM-like parameters (see Table 2), this approach allows us to fit the composite spectra of our subsamples. The Calzetti law appears to work quite well as an average attenuation law for large samples of high-redshift galaxies. Luminosity and SFR estimates derived by assuming the Calzetti law show good correspondence to values obtained by independent methods (e.g., Reddy & Steidel 2004; Erb et al. 2006b; Daddi et al. 2007b). Therefore, we assume that our modified Calzetti law describes, to zeroth order, on average dust attenuation in high-redshift star-forming galaxies with weak to moderate UV bumps. Characteristic values of x_0, γ, and c_3 are given in Table 2.

On the other hand, one may expect that the a priori use of a pure Calzetti law for fitting SEDs of any high-redshift galaxy introduces systematic errors whenever the extinction curve produced by dust in a galaxy exhibits a significant UV bump. As a test, we constructed synthetic SEDs that are consistent with our data using Maraston (2005) models reddened by a modified Calzetti law, according to a case "gm_sb" UV bump (see Table 2). The corresponding broad-band filter fluxes for different redshifts were then fitted by using the correct attenuation curve and a *pure* Calzetti law. The latter yielded about 5% higher masses and about 10% lower SFRs. For extreme but realistic cases, these discrepancies could be twice as large. The exact values depend on star-formation history, redshift (because of the differing filter coverage of the UV bump), and, of course, dust obscuration. The change in the rest-frame UV colours caused by the presence of a UV bump appears to be interpreted by a fitting routine that uses a standard Calzetti law as a signature of the older age of the stellar populations and/or a reduced dust reddening. For a typical high-redshift galaxy, the resulting deviations are almost negligible in view of the statistical and systematic uncertainties related to SED fitting in general. In the following sections, we therefore discuss fitting results with the *Hyperz* code based on a standard Calzetti attenuation law to be consistent with other studies. Nevertheless, one should keep in mind that, for objects with the strongest 2175 Å absorption features in their spectra, there could be noteworthy systematic deviations in the estimated galaxy properties.

4.3. Extinction curve and global properties of galaxies

4.3.1. Star-formation rates and stellar masses

Table 1 lists average values of several global galaxy properties for the three GMASS subsamples defined in Sect. 4.1. In general, the monochromatic luminosities at 1500 and 2500 Å (rest

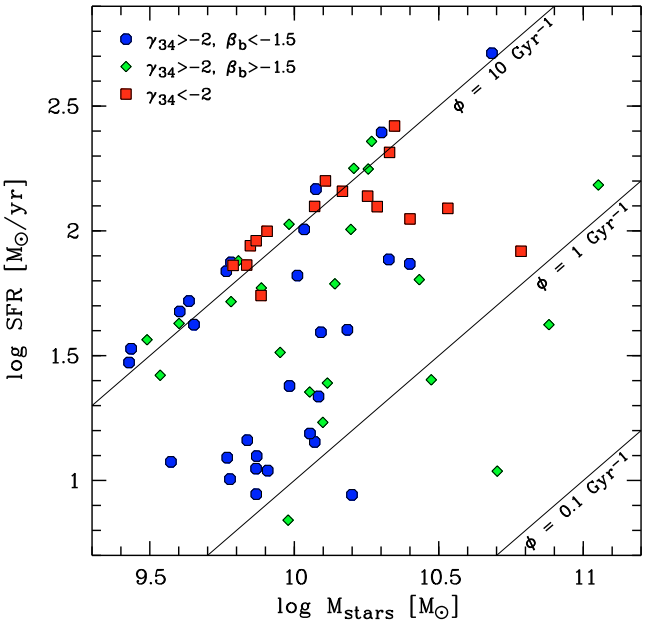

Fig. 10. Star-formation rate versus total stellar mass for the GMASS sample galaxies with $1.5 < z < 2.5$. The three γ_{34} and β_b selected subsamples are marked by different symbols (see legend). Specific SFRs of 10, 1, and 0.1 Gyr^{-1} are indicated by lines. The upper left corner of the diagram is not populated by galaxies because of the lower age limit of 100 Myr set for models with exponentially-declining SFRs for the SED fitting.

frame) of GMASS galaxies with a robustly identified 2175 Å absorption feature in their spectra do not differ from the average ones of the entire GMASS sample. However, some differences exist in terms of the specific star-formation rate ϕ, which is the SFR per unit total stellar mass $M_\star$ (derived from *Hyperz*, see Sect. 2.1), as shown in Fig. 10. In fact, GMASS SUBGs have $\langle M_\star \rangle = 1.4 \times 10^{10}\,M_\odot$ and $\langle SFR \rangle \sim 100\,M_\odot\,\mathrm{yr}^{-1}$, so that their values of ϕ cluster around 7.1 Gyr^{-1}. This is about twice the average ϕ of GMASS galaxies for which the signature of a UV bump in their spectra is weak or absent ($\langle\phi\rangle = 3.3$ Gyr^{-1}), whatever the observed UV slope. Interestingly, GMASS galaxies at $1.5 < z < 2.5$ with $\gamma_{34} > -2$ and blue UV continua tend to be less massive systems with lower SFRs than corresponding non-SUBGs with red UV continua.

A trend towards higher values of ϕ for SUBGs was also found by NPPS. We note that the GMASS galaxies at $1 < z < 2.5$ considered here are a factor of two less massive than the FDF galaxies at $2 < z < 2.5$ in the NPPS sample, but almost as massive as the FDF/K20 galaxies at $1 < z < 1.5$ in the NPPS sample. Consistently, for the entire 4.5 μm-selected GMASS sample, which also comprises galaxies with photometry only and spectroscopic redshifts from other projects in GOODS-S, the average stellar mass drops from ~2.4 to ~$1.0 \times 10^{10}\,M_\odot$ moving from $2 < z < 2.5$ to $1 < z < 1.5$, if $SFR \geq 10\,M_\odot$/yr (lower limit for our spectroscopic sample). Apart from different sample selection criteria and different methods of estimating stellar masses[7], the average sample masses probably decrease towards lower redshifts due to the increasing fraction of low-mass objects in flux-limited samples and a decrease in the number density of massive

[7] Comparison of stellar masses for galaxies in both samples suggests that the values used by NPPS are systematically higher by about 0.1 dex, which is probably in general due to the different assumptions about the SFH (see also Drory et al. 2005).

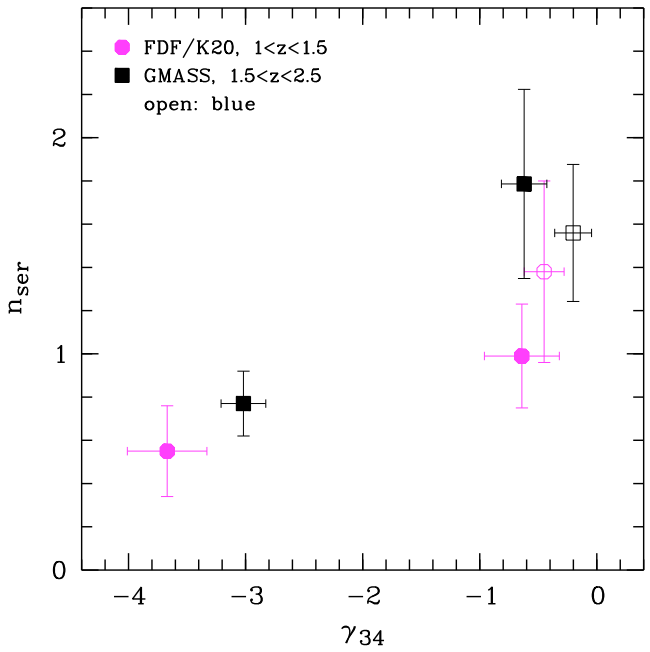

Fig. 11. Sersic index n_{ser} versus γ_{34} for the three GMASS subsamples at $1.5 < z < 2.5$ and three subsamples of FDF and K20 galaxies at $1 < z < 1.5$ discussed by NPPS. The link between subsamples and symbols is illustrated in the legend. Open symbols indicate subsamples of galaxies with blue UV continua and weak 2175 Å features. Errors represent sample mean errors.

star-forming galaxies related to the "downsizing effect" (Cowie et al. 1996; Gavazzi & Scodeggio 1996; Gavazzi et al. 1996).

4.3.2. Morphology

Quantitative morphological studies of galaxies at $z \sim 2$ can be significantly affected by the relatively low surface brightness of, in particular, their outer regions, which can lead to erroneous morphological classifications. However, extremely deep ACS exposures are available for GOODS-South (see Sect. 2.1), which allow us to analyse the rest-frame UV/U-band surface brightness distribution of our sample galaxies at least in an approximate way. Table 1 shows the results for the effective radius r_e, Sérsic index n_{ser}, elongation b/a, and the CAS parameters concentration C and asymmetry A (see Cassata et al. 2005, for the definitions used) for our three GMASS samples at $1.5 < z < 2.5$.

In general, the derived morphological parameters do not depend significantly on the UV continuum properties. A remarkable exception is the average Sérsic index for GMASS SUBGs $\langle n_{ser} \rangle = 0.77 \pm 0.15$, which is conspicuously lower than the values 1.56 ± 0.32 and 1.79 ± 0.44 for coeval non-SUBGs with blue and red UV continua, respectively. Consequently, SUBGs appear to show radial distributions of the young stellar populations that are on average shallower than an exponential profile. On the other hand, half of the SUBGs have the minimum value allowed for the fit $n_{ser} = 0.5$, which challenges the reliability of the fits. Moreover, there is no significant difference between our three GMASS subsamples in terms of the concentration C, which also depends on the radial surface brightness profile. However, this dependence is different, since C is related to the ratio of the apertures containing 80% and 20% of the total flux, while n_{ser} describes the functional form of the radial light distribution. The concentration C is obviously less sensitive to the substructure of the radial profile than n_{ser}, which appears to indicate irregular, very patchy rest-frame UV surface brightness profiles for low Sérsic indices. A good argument for the reliability of the observed γ_{34}-related trend in n_{ser} is the result that a similar relation is present in the intermediate-redshift NPPS sample at $1 < z < 1.5$ (see Fig. 11). Even if the physical interpretation of the n_{ser} values is difficult, the significance of the observed trend could in principle be used to search (in combination with other tracers) for SUBG candidates without available deep UV spectroscopy.

The use of the CAS parameters for galaxy classification (see Conselice et al. 2003) shows that the GMASS galaxies at $1.5 < z < 2.5$ appear to be a fair mixture of mergers/irregulars and disc galaxies, whatever γ_{34}. This distribution differs significantly from the one at $1 < z < 1.5$, where most of the SUBGs appear to have late-type morphologies (see NPPS). Since mergers are frequent in the NPPS sample of SUBGs at $2 < z < 2.5$, this suggests that the distribution of the young stellar populations in galaxies with LMC-like dust becomes smoother as time goes by.

Table 3. Rest-frame equivalent widths in Å of prominent lines in the composites of the three GMASS subsamples at $1.5 < z < 2.5$.

Line	Type[a]	$\gamma_{34} > -2$ $\beta_b < -1.5$	$\gamma_{34} > -2$ $\beta_b > -1.5$	$\gamma_{34} < -2$
Si IV λ 1400	is	$+3.18 \pm 0.50$	$+2.90 \pm 0.63$	$+4.06 \pm 0.75$
S V λ 1502	s	$+0.55 \pm 0.09$	$+0.60 \pm 0.07$	$+0.83 \pm 0.11$
Si II λ 1526	i	$+1.97 \pm 0.12$	$+1.95 \pm 0.17$	$+2.73 \pm 0.28$
C IV λ 1550	si	$+4.48 \pm 0.36$	$+4.52 \pm 0.54$	$+5.65 \pm 0.32$
Fe II λ 1608	i	$+1.36 \pm 0.15$	$+1.72 \pm 0.12$	$+1.72 \pm 0.27$
He II λ 1640	sn	-1.14 ± 0.27	-1.23 ± 0.35	-1.29 ± 0.28
Al II λ 1670	i	$+1.43 \pm 0.08$	$+1.53 \pm 0.14$	$+2.04 \pm 0.18$
Al III λ 1860	i	$+2.61 \pm 0.20$	$+3.11 \pm 0.22$	$+3.66 \pm 0.20$
C III] λ 1907	n	-1.05 ± 0.14	-1.48 ± 0.14	-1.16 ± 0.22
C II] λ 2326	n	-1.03 ± 0.22	-1.63 ± 0.21	-0.92 ± 0.21
Fe II λ 2344	i	$+1.97 \pm 0.35$	$+2.07 \pm 0.19$	$+2.95 \pm 0.26$
Fe II λ 2380	i	$+3.16 \pm 0.32$	$+3.67 \pm 0.24$	$+4.83 \pm 0.29$
Fe II λ 2600	i	$+4.79 \pm 0.48$	$+5.15 \pm 0.62$	$+5.85 \pm 0.68$
Mg II λ 2800	is	$+4.01 \pm 0.75$	$+4.02 \pm 0.73$	$+6.59 \pm 0.76$
Mg I λ 2852	s	$+0.30 \pm 0.19$	$+0.83 \pm 0.25$	$+1.30 \pm 0.34$

[a] Line origin: s = stellar (photosphere and/or wind), i = interstellar absorption, n = nebular emission.

4.3.3. Narrow spectroscopic features

In the rest-frame UV domain mapped by the composite GMASS spectra, we can study 15 well-detected spectral lines from Si IV λ 1400 to Mg I λ 2852 (see Table 3). The most prominent features are interstellar absorption lines and/or originate in stellar winds, and often show P Cygni profiles. Equivalent widths (EWs) and their uncertainties are reproduced in Fig. 12, as well as relative EWs with respect to the GMASS subsample of galaxies at $1.5 < z < 2.5$ with $\gamma_{34} > -2$ and red UV continua. Comparison of the 12 absorption-dominated spectral lines of the GMASS blue and red subsamples of non-SUBGs reveals that the former type of galaxies has weaker features by only 11 (±5)% on average. In contrast, GMASS SUBGs exhibit stronger features, on average, by 34 (±5)%. On the other hand, the GMASS red subsample of galaxies with $\gamma_{34} > -2$ tend to have stronger emission-dominated lines than the others by 20–30%. However, these emission lines have relatively uncertain EWs due to their weakness, even in composite spectra.

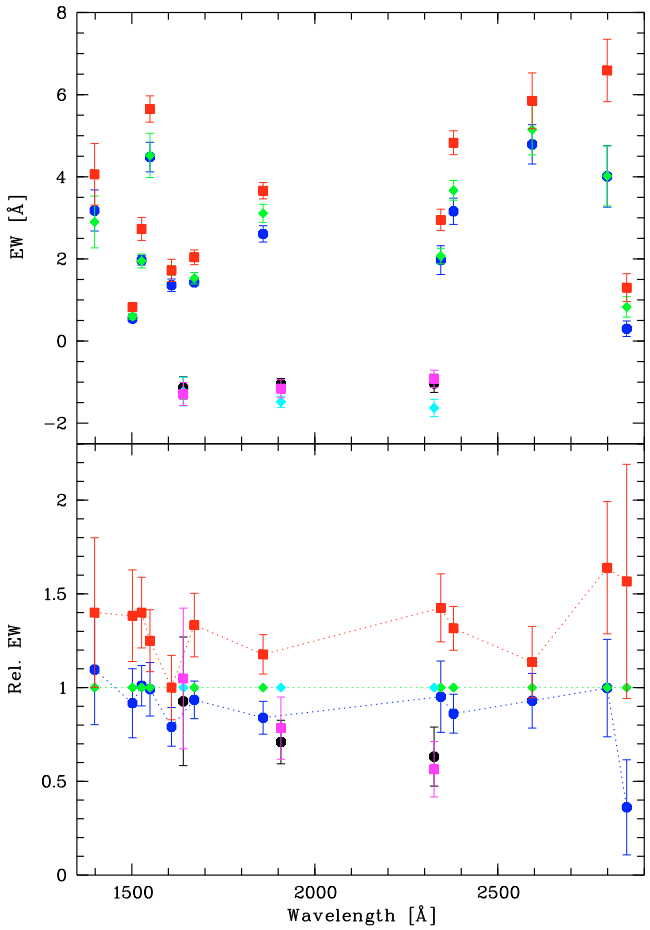

Fig. 12. Rest-frame equivalent widths of 15 spectral lines between 1350 and 2900 Å for the composite spectra of three GMASS subsamples at $1.5 < z < 2.5$. Circles and lozenges mark blue and red galaxies with $\gamma_{34} > -2$. Squares indicate galaxies with $\gamma_{34} < -2$. The 1σ error bars include the variance between the individual spectra, the errors of the continuum level definition, and the statistical uncertainties of the line strengths. *Upper panel*: absolute equivalent widths in Å. Emission lines have negative EWs. *Lower panel*: equivalent widths relative to the values for the red subsample with weak 2175 Å absorption features. Uncertainties on the reference values are considered by the error bars of the other samples. The relative EWs of the absorption-dominated lines of each subsample are connected by dotted lines in order to guide the eye.

Hence, we confirm that galaxies with secure detections of a broad absorption feature centred on 2175 Å in their spectra exhibit stronger low-ionisation interstellar absorption lines than those with a probable SMC-like extinction curve (NP05). This was interpreted as being due to a higher covering fraction of dusty neutral clouds in the former galaxies, which enables the carriers of the UV bump to survive. In this case, the low-ionisation interstellar lines trace the distribution of neutral gas clouds along the observer's sightline towards the hot stars producing the illuminating UV continuum radiation (Shapley et al. 2003). An alternative explanation for the presence of stronger interstellar absorption lines is a broader velocity distribution (see Heckman et al. 1998).

In addition, Fig. 12 reveals that, in galaxies with a signature of a UV bump in their spectra, stronger absorption is inferred from all types of absorption lines, regardless of the wavelength and ionisation level. Hence, the higher absorption efficiency must be explained also for line components originating in stellar photospheres and winds. An enhanced metallicity is a likely interpretation. Since the strengths of wind features depend on metallicity (e.g., Leitherer et al. 2001; Mehlert et al. 2002), a higher metallicity could explain (at least in part) the significant absorption in the C IV λ 1550 Å feature of SUBGs (cf. NP05). At least for the red galaxies in our sample, this interpretation is supported by the corresponding presence of UV nebular emission lines of lower strength (see Heckman et al. 1998; Noll et al. 2004) in the spectra of the same $\gamma_{34} < -2$ galaxies.

Unfortunately, a determination of metallicity for the composite spectrum of each GMASS subsample considered here is not possible. Halliday et al. (2008) were able to determine a stellar metallicity equal to $\sim 0.3\,Z_\odot$, based on the weak stellar Fe III λ 1978 Å index (Rix et al. 2004), for a composite spectrum combining 75 galaxy spectra from the entire GMASS survey. This iron-abundance, stellar metallicity is lower than the oxygen-abundance, gas-phase metallicity determined for UV-selected star-forming galaxies at $z \sim 2$ (Erb et al. 2006a), and metallicities determined for hot stars (Mehlert et al. 2002, 2006) and the ISM (Savaglio et al. 2004) in galaxies at similar redshifts, which exhibit values $\gtrsim 0.5\,Z_\odot$. Halliday et al. (2008) concluded that a light-element overabundance was being established in the selected GMASS star-forming galaxies as they were forming at $z \sim 2$. The higher EW of the Mg I λ 2852 Å line measured in GMASS galaxies that probably host the carriers of the UV bump could be explained by a higher fraction of intermediate-age stars (cf. NPPS). Unfortunately, uncertainties prevent us from establishing any difference in either the measured Mg-to-Fe EW ratio or the properties of the stellar populations (from our models) among our GMASS subsamples for $1.5 < z < 2.5$. Nevertheless, we note that the stellar metallicities of our star-forming, intermediate-mass galaxies at $1.0 < z < 2.5$ are not far from those of LMC stars.

4.4. Dust grain populations emitting at mid-IR wavelengths

The carriers of the UV bump probably consist of organic carbon and amorphous silicates (Bradley et al. 2005, and references therein), and seem to populate different environments of their host galaxy (see, e.g., Whittet 2003; Gordon et al. 2003; Fitzpatrick 2004; Clayton 2004, and references therein). Another component of the dusty ISM, which is ubiquitous and also consists of carbonaceous material, is represented by the large polycyclic aromatic hydrocarbon (PAH) molecules (see Peeters et al. 2004, and references therein). Far-UV pumped, vibrational emission of PAHs is generally held responsible for the well-known emission features at 3.3, 6.2, 7.7, 8.6, and 11.2 μm, which dominate the mid-IR spectra of many objects with associated dust and gas (Léger & Puget 1984; Allamandola et al. 1985, 1989; Puget & Léger 1989; Tielens et al. 1999, 2000). Unfortunately, there is no mid-IR spectroscopy for the GMASS sample, so that the physical conditions in the global environment where PAHs and the carriers of the UV bump exist cannot be inferred either quantitatively or qualitatively (from the comparison with the spectra of nearby objects). However, we can at least use the emission in the broad-band MIPS 24 μm filter to estimate the alleged PAH emission around $\sim 8\,\mu$m (rest frame).

Observations in the MIPS 24 μm filter are available for the 68 GMASS galaxies under study: fluxes range from 6 to 410 μJy, 14 galaxies being 2σ detections, and an additional four having only 3σ upper limits. Interestingly, the four galaxies without detection exhibit $\gamma_{34} > -2$ and $\beta_b < -1.5$. The MIPS 24 μm fluxes

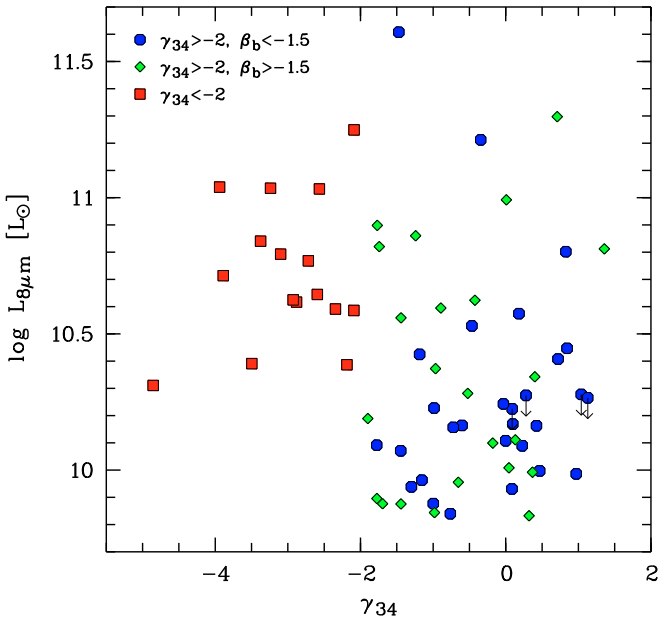

Fig. 13. Rest-frame luminosity at about 8 μm $L_{8\,\mu m}$ versus γ_{34} for the three GMASS subsamples at $1.5 < z < 2.5$ (see legend for the symbols). Arrows indicate objects with 3σ upper flux limits only.

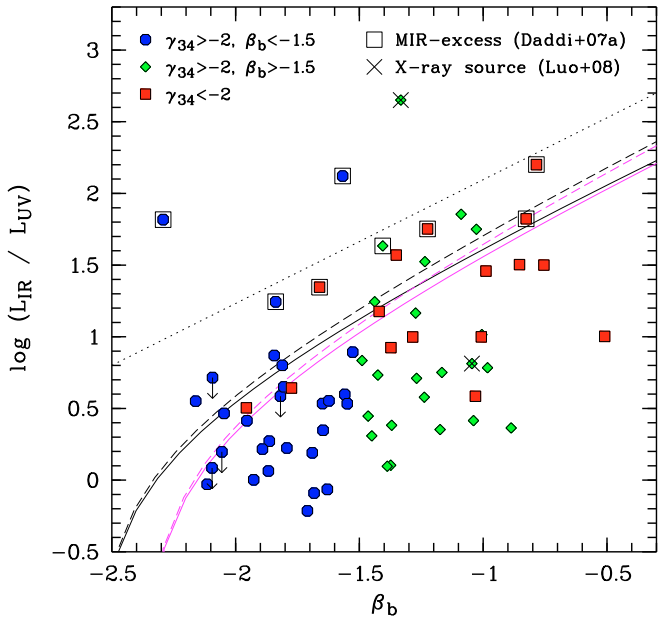

Fig. 14. Ratio of the IR luminosity L_{IR} and the UV luminosity L_{UV} versus the UV-continuum reddening measure β_b for the three GMASS subsamples at $1.5 < z < 2.5$ (see legend for the symbols). L_{IR} is derived from the 24 μm fluxes by using the Dale & Helou (2002) models, while L_{UV} is derived from SED fitting in the wavelength range below 3000 Å. Galaxies that show particularly high luminosity ratios in comparison to other galaxies with similar β_b are separated by a dashed line. The mid-IR-excess objects of Daddi et al. (2007a) are indicated by big open squares. X-ray sources in the catalogue of Luo et al. (2008) are marked by big crosses. The X-ray source above the dotted line is not part of the Daddi et al. (2007a) sample. Theoretical curves are given for solar-metallicity Maraston (2005) models with either continuous SFR and age of 100 Myr (black) or with $\tau = 3$ Gyr e-folding time SFR and age of 3 Gyr (magenta or grey). Solid lines are for a pure Calzetti et al. (2000) law. Dashed lines show the results for a Calzetti law plus the "gm_sb" UV bump in Table 2.

are converted into rest-frame luminosities at ~8 μm, where $L_{8\,\mu m}$ is calculated from the filter-averaged νf_ν (cf. Daddi et al. 2007a). Relatively small cosmological k-corrections are obtained from the Dale & Helou (2002) IR templates, which are parameterised by the slope of the power-law distribution of dust mass over heating intensity α[8]. Of the GMASS UV-luminous, intermediate-mass galaxies at $1.5 < z < 2.5$, those with a signature of the UV bump in their spectra appear to be more luminous (by ~0.4 dex) at ~8 μm (rest frame) than the other galaxies, even if only objects with similar UV-continuum reddening ($\beta_b > -1.5$) and stellar mass (cf. Table 1) are considered (see Fig. 13). The 8 μm luminosities of the former galaxies are basically above $2 \times 10^{10}\,L_\odot$.

For a clearer understanding of these results, we show the diagnostic diagram defined by the luminosity ratio L_{IR}/L_{UV}[9] and the UV-continuum slope β_b for the 68 GMASS galaxies at $1.5 < z < 2.5$ under study in Fig. 14. Most of these galaxies are either located along the locus of nearby starbursts (cf. Meurer et al. 1999) or populate the region below this locus, where nearby "normal" star-forming galaxies lie (e.g., Kong et al. 2004; Buat et al. 2005; Panuzzo et al. 2007). According to the interpretations given by the previous authors, the scatter of the GMASS SUBGs across the locus of nearby starbursts (the so-called "Meurer law", see Meurer et al. 1999) is consistent with the simple dust-screen model described in Sect. 4.1. At the same time, the location of (red) galaxies with $\gamma_{34} > -2$ in Fig. 14 could indicate that the observed UV bumps are weakened due to more complex dust/star distributions (see NPPS for a detailed discussion).

The a priori exclusion of optically identified AGN, still allows the presence of continuum emission at mid-IR wavelengths caused by deeply obscured non-thermal sources. However, only two galaxies among the GMASS galaxies plotted in Fig. 14 have been detected in X-rays: none of them exhibits a significant UV bump. In fact, a non-detection in X-rays does not exclude a hidden AGN being present in our sample, as the X-ray stacking analysis of Daddi et al. (2007b) indicates. Indeed, hidden AGN candidates identified as "IR-excess objects" (see Daddi et al. 2007a) are present among GMASS galaxies at $1.5 < z < 2.5$ with $\gamma_{34} < -2$ (25%) or with $\gamma_{34} > -2$ (10%)[10]. However, the moderate L_{IR}/L_{UV} for most of the GMASS galaxies in Fig. 14 suggest that the measured MIPS 24 μm fluxes are mainly associated with PAH emission and star formation. Moreover, our three GMASS subsamples do not show suspicious values and significant differences in IRAC colours that can discriminate between galaxies dominated by star formation and by AGN in the rest-frame near-IR (see Lacy et al. 2004; Stern et al. 2005; Pope et al. 2008). For example, SUBGs and non-SUBGs show on average $S_{8.0}/S_{4.5} = 0.8$ and no SUBG was found to be located above the Pope et al. (2008) AGN criterion of 2.0. Finally, the Teplitz et al. (2007) *Spitzer* IRS spectrum (source 2 in their Fig. 5) of the galaxy in the NPPS sample with the strongest 2175 Å feature,

[8] Templates are chosen according to the mean relation between α (or f_ν^{60}/f_ν^{100}) and the IR luminosity derived by Marcillac et al. (2006) for local IR-luminous galaxies. We note that the Dale & Helou (2002) IR templates exhibit only small differences at 8 μm (rest frame), so that small uncertainties are propagated to $L_{8\,\mu m}$.

[9] L_{IR} is derived from the measured MIPS 24 μm fluxes by the adoption of the Dale & Helou (2002) templates and the calibration of Marcillac et al. (2006). L_{UV} is measured in the best-fit SED of *Hyperz* at wavelengths below 3000 Å.

[10] One of the latter objects is actually part of the GOODS-S X-ray catalogue of Luo et al. (2008, see Fig. 14).

a K20 galaxy at $z = 1.097$, indicates a typical, star-formation-dominated, luminous infrared galaxy. Unfortunately, this convincing check cannot be performed for other sample galaxies because of the lack of published mid-IR spectroscopy.

Additional support against an AGN-related origin of the observed mid-IR emission comes from the stacking analysis of MIPS fluxes in the 70 μm filter for the three GMASS subsamples (Elbaz & Magnelli, priv. comm.). As a result, only 3σ upper limits between 600 and 800 μJy are obtained. This excludes the suitability of Dale & Helou (2002) IR SEDs with power-law slopes of the dust mass distribution over heating intensity $\alpha < 1.2$, which peak at wavelengths <63 μm in f_ν and are more extreme than SEDs of typical star-forming galaxies (Dale & Helou 2002). The typical values of α that we determine from the MIPS 24 μm fluxes and the calibration of Marcillac et al. (2006) are about 1.7−1.8.

We can therefore safely conclude that the bulk of the observed MIPS 24 μm flux of the GMASS galaxies under study comes from PAH emission, this emission being higher for objects with relatively strong 2175 Å absorption features in their spectra. This enhanced PAH emission is probably due to at least one of the following reasons: 1) a higher abundance of PAHs or a larger amount of dust; 2) a more efficient attenuation by dust as a result of the dust/star distribution (see NPPS for a discussion); 3) a stronger illuminating radiation field, as a consequence of a larger UV throughput or a reduced dilution (i.e., increased closeness of dust to illuminating stars). All of these independent interpretations are supported by our data to some level. In particular, the relation between the 8 μm emission and the SFR or ϕ (see Table 1) suggests a link between star-formation intensity and the amount of dust in the galaxy (cf. Wang & Heckman 1996; Vijh et al. 2003).

5. Discussion

We have investigated spectral evidence of the broad absorption feature centred on 2175 Å, following the method developed by NP05. The NPPS main sample of 88 actively star-forming, intermediate-mass (i.e., with average stellar masses of 10^{10}–10^{11} $M_\odot$) galaxies at $1 < z < 2.5$ with appropriate spectra was enlarged by considering 68 GMASS galaxies at $1.5 < z < 2.5$. The gain consists not only in the larger size and the more homogeneous redshift coverage of the new sample. The additional GMASS galaxies have particularly high S/N optical spectra that bracket the redshifted wavelength region across the UV bump, so that a Lorentzian-like fitting of this broad feature can be performed. This allows us to study the shape of the UV bump and the link between its spectral signature (i.e., the parameter γ_{34} introduced by NP05) and the properties (e.g., central wavelength and *FWHM*) of the fitted UV bumps. Furthermore, the GMASS sample is large enough to enable subsampling: in composite spectra of sufficiently high S/N, EWs can be measured more robustly for many narrower spectral features than in previous studies. These absorption/emission lines originate in very different local environments, such as stellar photospheres, wind regions, nebular regions, and the ISM. Finally, available MIPS 24 μm observations allow us to estimate the total amount of emission by dust at IR wavelengths and constrain the opacity characterising different GMASS subsamples. Hereafter, we discuss our main results in terms of galaxy structure, and the evolution of stellar populations and the ISM.

5.1. Differing extinction curves in high-redshift galaxies

We have produced robust evidence that at least 30% of the UV-luminous, intermediate-mass galaxies at $1 < z < 2.5$ contain dust that produces an extinction curve with a broad absorption excess centred on 2175 Å that differs from the standard SMC curve at UV wavelengths[11]. We refer to these objects, identified by $\gamma_{34} < -2$, as *s*ignificant *U*V *b*ump *g*alaxies (SUBGs). With the exception of our previous investigations (NP05; NPPS), the presence of the carriers of the UV bump in statistical samples of galaxies has been limited so far to intervening Ca II and possibly Mg II absorbers at intermediate/high redshifts (Malhotra 1997; Wang et al. 2004; Wild & Hewett 2005). Our results imply that a non-negligible fraction of the observed actively star-forming galaxies at $1 < z < 2.5$ already has a UV extinction curve that differs from that characterising LBGs at similar and higher redshifts (cf. Vijh et al. 2003). UV extinction curves in-between the average SMC one (with no UV bump but a steep far-UV slope) and the average LMC one (with a moderate UV bump and a less steep far-UV slope) appear to be common, whereas the average MW extinction curve (with a prominent UV bump and a less steep far-UV slope) does not. In particular, the shape of the UV bump inferred from the composite spectrum of SUBGs in the GMASS sample resembles that measured in the "supergiant" shell of ionised filaments LMC 2, close to 30 Dor[12].

Both the fraction of actively star-forming galaxies at $1 < z < 2.5$ with alleged UV bumps in their spectra, and the type of extinction curve (e.g., LMC versus MW average ones), depend on the dust/star distribution, which is generally unconstrained by existing observations of high-redshift galaxies (NPPS). Extinction curves with a moderate UV bump are favoured if dust is mainly distributed above stars, as suggested for SUBGs, which are indicative of high covering fractions of young massive stars due to large EWs of strong interstellar absorption lines (Fig. 12). Moreover, the distribution of GMASS SUBGs in the β_b–L_{IR}/L_{UV} plane (Fig. 14) is aligned mainly along the opacity-dependent Meurer curve (Meurer et al. 1999) for starburst models with screen-like dust attenuation. Dust screens are expected if winds on a galactic scale or more localised superwinds are present (see, e.g., Murray et al. 2005). Galactic outflows are ubiquitous, particularly at high redshift (e.g., Weiner et al. 2009; see Heckman 2005; and Veilleux et al. 2005, for reviews). The presence of galactic winds or localised superwinds in GMASS galaxies, for instance, is supported by the high values of the specific SFR (Fig. 10). Part of the expelled dust grains may settle in a potential minimum within the galaxy halo, as a result of simple dynamical arguments about the motion of interstellar grains out of the galactic disc (Greenberg et al. 1987; Barsella et al. 1989; Ferrara et al. 1990, 1991; Davies et al. 1998). The presence of poloidal magnetic fields may help to confine expelled dust grains (Beck et al. 1994), and, thus, preserve the SHELL-like configuration for the dust/star distribution that can describe dust attenuation in nearby and high-redshift starbursts (see Witt & Gordon 2000; Vijh et al. 2003). Increasing observational evidence points to the existence of organised magnetic fields in and around galaxies without AGN activity at intermediate/high redshifts, which are at least of comparable strength

[11] Sample selection criteria and survey sensitivity can hinder this fact, as suggested by NPPS.

[12] This supergiant shell probably results from the combined action of stellar winds and supernova explosions over a timescale of 10^7 yr (Caulet et al. 1982) and a unique magnetic field geometry, consisting of coherent fields on spatial scales of 42 × 24 pc to 104 × 83 pc with inferred projected field strengths of ∼14−30 μG (Wisniewski et al. 2007).

to those observed in nearby normal galaxies (Bernet et al. 2008; Wolfe et al. 2008).

A higher fraction of objects can host the carriers of the UV bump, if dust is distributed mainly in the plane of the galaxy (as, e.g., in the radiative transfer models presented in Silva et al. 1998; and Pierini et al. 2004b). As shown by NPPS, a disc system with a MW extinction curve then exhibits $-3 < \gamma_{34} < 1$ only. The fraction of dust above the mid-plane of a galaxy can decrease as the SFR per unit area of the galaxy decreases (cf. Heckman 2005). Disc-dominated dust distributions become more likely as the cosmic SFR density decreases, i.e., towards redshifts progressively lower than unity (Madau et al. 1996). On the other hand, extinction curves more similar to those of the LMC or MW are also possible, if the dust/star distribution is patchy on very large scales (see NPPS) or depends on the age of the individual stellar populations (see Panuzzo et al. 2007). These dust/star distributions appear to explain the position of "normal" star-forming galaxies distinctly below the Meurer curve (Meurer et al. 1999; Kong et al. 2004; Buat et al. 2005), where many non-SUBGs in our sample are located (see Fig. 14).

Finally, we note that the extinction properties inferred in this study and in our previous ones refer to a galaxy-averaged environment. It is well known from studies of the MW, LMC, and SMC that bulk dust properties vary on much smaller scales than a galaxy scale length (down to sub-pc). Hence, the carriers of the UV bump may exist in particular regions of galaxies that do not exhibit spectral evidence of the 2175 Å feature. This may explain why a typical LMC extinction curve has so far been inferred only for the sightline towards GRB 070802 at $z = 2.45$ (Elíasdóttir et al. 2008), whereas GRB-host galaxies are commonly assumed to host SMC-like dust. It is clear that the stardust yields and the processes of creation and transformation of dust species and sizes in the general ISM play a fundamental role in explaining the variety of extinction curves in different galaxy environments. This is discussed in the next section.

5.2. The carriers of the UV bump and other small-size dust components at high redshifts

Some forty years after the discovery of the UV bump, proposals about the chemical composition of its carriers remain largely conjectural. If the observed properties of the UV bump strongly suggest that its carriers are in the small particle limit (i.e., $a \ll \lambda$), the abundance argument limits the set of possible constituent elements to C, Mg, Si, and Fe. Graphitic carbon is by far the most widely discussed and accepted material among these candidates, since it is the only one to exhibit a broad excess in the absorption cross-section at UV wavelengths (see Papoular & Papoular 2009, for a recent discussion). However, as for any material, its properties must explain the variations in width of the UV bump, whilst conserving its peak wavelength (Whittet 2003)[13]. The random, hydrogen-free assembly of microscopic sp^2 carbon chips forming a macroscopically homogeneous and isotropic solid, which was proposed as a model carrier of the UV bump (Papoular & Papoular 2009), is able to explain these properties taking into account astrophysical conditions in the ISM. The most promising, alternative carbon-based materials are synthetic nanoparticles condensed in a hydrogen-rich atmosphere and polycyclic aromatic hydrocarbons (PAHs), which exhibit a rise in the absorption cross-section across the region in which the UV bump originates. In addition, oxygen-rich materials have been proposed as carriers of the UV bump. In particular, silicate-based materials appear the most probable candidates, although this may require unreasonable fine-tuning of the size distribution (Whittet 2003). If graphitic grains (at least partly) are responsible for the UV bump, the main effect of the presence of PAHs (and probably silicates) will be then to increase the absorption cross section in particular at the wings of the UV bump, causing the feature to become less prominent. A variable mixture of the three components could explain variations in the height and width of the UV bump among observed extinction curves. Thus, it is safe to assume that the carriers of the UV bump are a mixture of amorphous silicates and carbonaceous material, as indeed observed in solar-system interplanetary particles (Bradley et al. 2005)[14].

According to the successful dust model of Désert et al. (1990), the far-UV non-linear rise in the extinction curve can be ascribed mostly to large molecules (radius $a \sim 0.4-1$ nm), i.e., PAHs, whereas carbonaceous nanoparticles ($a \sim 1-10$ nm) called very small grains (VSGs) are responsible for the sharp absorption excess at 2175 Å, and big grains (BGs, $a \sim 10-100$ nm) cause most of the extinction at UV wavelengths, but in a featureless way and with decreasing efficiency from the near- to the far-UV domain. Furthermore, PAHs are the carriers of the aromatic infrared bands between 3 and 17 μm, whereas VSGs are responsible for the continuum emission at mid-IR wavelengths. Differences in the far-UV slope and/or the strength of the UV bump are related to zeroth order differences in the fraction of big grains and in the VSG-to-PAH abundance ratio of the dust. The latter arise from both dust production, either in stellar outflows (i.e., stardust) or in the general ISM, and dust processing in the general ISM (Whittet 2003, and references therein). Regardless of whether the carriers of the UV bump originate in stars, the main unknown is the abundance required to alter in the appropriate way the shape of the average extinction curve of a galaxy.

Silicates (mostly amorphous) are produced in outflows of oxygen-rich cold stars, such as O-rich asymptotic giant branch (AGB) stars and red giant and supergiant stars (Whittet 2003, and references therein). In contrast, amorphous carbonaceous grains and PAHs are produced in outflows of carbon-rich cold stars, i.e., AGB carbon stars[15]. In any event, intermediate-mass stars ($1 < M < 8\,M_{\odot}$) lose most of their mass during their AGB phase (e.g., Iben & Renzini 1983). Hence, they are major producers of dust grains, possibly including those responsible for the UV bump. Besides the winds of AGB stars, the expanding envelopes of Type II supernovae (SNe) represent an

[13] The width of the UV bump possibly varies owing to different mechanisms, including particle clustering, ice-mantle growth, compositional inhomogeneities, porosity variations, and surface effects. Our data do not give us a handle on any of these processes; however, we expect less particle clustering and mantle growth in carriers that are above the mid-plane of the galaxy (as in SUBGs), since the two phenomena take place in regions like molecular clouds, protostellar discs, etc.

[14] Carbon-rich and silicate materials are made in different circumstellar environments (see text later on). How and where the two components, originating in different production sites, were combined within the same dust particles remains unclear. Hence it is uncertain whether the history of solar-system particles can be regarded as typical of those in remote galaxies. Moreover, Bradley et al. (2005) could not distinguish whether the UV bump is due to organic carbon or amorphous silicates (or both), nor could exclude other possible UV-bump carriers.

[15] The amorphous carbon grains ejected by C-rich stars need to be at least partly graphitised by interstellar processes to produce the distinctive absorption feature at 2175 Å (Whittet 2003, and references therein). This would take about 100 Myr if such a process is driven by UV radiation (see Sorrell 1990; Mennella et al. 1996, 1998).

O-rich environment where silicate dust can form (Whittet 2003). According to Zhukovska et al. (2008), SNe could also be important for the production of carbon dust, mostly in crystalline form (i.e., graphitic-like). In any case, the importance of SNe for the dust production in galaxies is still highly uncertain (Bianchi & Schneider 2007, and references therein). AGB stars and their outflows appear with a short delay after the beginning of star formation, i.e., some ~30 Myr, which is the lifetime of a $8\,M_{\odot}$ star. AGB stars more massive than $\sim 3\,M_{\odot}$ never become carbon stars (e.g., Renzini 2008, and references therein), can hence potentially produce silicate stardust but not C-rich stardust. For the latter grains to appear, one needs to wait for stars less massive than $\sim 3\,M_{\odot}$ to reach the AGB, or ~300 Myr after the beginning of star formation. Moreover, low metallicity favours the appearance of carbon stars, because less carbon needs to be dredged up in AGB stars to reach C/O ratios of above unity, and turn them into carbon stars (Renzini & Voli 1981). In summary, the theory of stellar evolution foresees that silicates are more promptly released than carbon-rich grains, and carbon grains are more abundantly produced in a low-metallicity environment.

With the persistent uncertainty in the chemical nature of the UV-bump carriers, their stellar producers, and their possible reprocessing in the general ISM, much of the following discussion is speculative. It is safe to say that the EWs of several emission/absorption features of carbon and silicon imply that the chemical enrichment of these dust constituents has proceeded significantly in the SUBGs in our GMASS sample (see Table 3). Additional evidence is provided by the emission at $8\,\mu$m (rest frame), if this emission is dominated by PAHs. In particular, emission features around $8\,\mu$m (rest frame) are associated with C-rich stars (Whittet 2003, and references therein). Thus, AGB outflows probably play a dominant role in the build-up of the carriers of the UV bump in massive galaxies at high redshift (NP05; NPPS), as well as in the build-up of PAHs in local (Galliano 2008) and high-redshift galaxies alike. Consistently, dust exclusively formed in the ejecta of core-collapse SNe and exposed to sputtering by the hot gas appears to produce extinction curves that do not exhibit a UV bump (see Bianchi et al. 2007; Nozawa et al. 2008, and references therein).

The absence of the UV bump in the SMC challenges the idea that carbon grains represent its carriers, since the SMC is very rich in carbon stars and yet no UV bump is present there. The lack of a UV bump could also be caused by efficient grain destruction (Gordon et al. 2003; Sloan et al. 2008) favoured by lower dust column densities and harder radiation fields due to the low metallicity. If carbonaceous carriers of the UV bump are more sensitive to harsh environments than silicate ones, then the UV bump strength may be lower in carbon-dust dominated low-metallicity environments than in high-metallicity galaxies, where the dominant population of silicates may also act as carriers of the UV bump. The latter is possible for our sample of SUBGs (cf. Sect. 4.3.3). On the other hand, these galaxies appear to contain a large amount of PAHs (see Sect. 4.4), which are carbonaceous in nature.

The destruction of refractory dust proceeds predominantly in the intermediate warm phase of the ISM (McKee 1989; Jones et al. 1994). This phase of the ISM has probably a large filling factor in actively star-forming galaxies at high redshift. In the low-density phases of the ISM, where SN explosions generally occur (at least in the local Universe), the relative abundance of PAHs with respect to VSGs is higher than in the high-density phases of the ISM. This was also found to be true for the diffuse, illuminated part of dense photodissociation regions (Compiégne et al. 2008), whose chemistry is controlled by the external UV radiation field. Thus, we can assume that, in diffuse (dense) regions of the ISM of UV-luminous, massive galaxies at high redshift, narrow (broad) UV bumps are observed as a consequence of the higher (lower) fraction of PAHs. This trend is observed in the MW (Fitzpatrick & Massa 1986; Cardelli & Clayton 1991; Valencic et al. 2004), although it is usually explained in terms of ice mantle growth in the dense regions (Mathis 1994). Unfortunately, a similarly clear trend has not been observed in the LMC (Misselt et al. 1999). On the other hand, different dust components may have different spatial distributions on scales ranging from pc to kpc, and, thus, be exposed to different stresses caused by the UV radiation field and shocks. Unfortunately, the few existing computations of dust expulsion and erosion reach conflicting conclusions about the distances at which graphite and silicate grains are located and the equilibrium distances reached by grains of different sizes (cf. Bianchi & Ferrara 2005; Aguirre et al. 2001, 2001). Our analysis suggests that carriers of the UV bump populate regions at some distance from the mid-plane of a galaxy at least in SUBGs. They might have survived expulsion or been produced by erosion during expulsion of larger carbonaceous grains.

Whatever the carriers of the UV bump are, it is reasonable to expect that a higher fraction of them are hosted by more evolved galaxies at high redshift. If they are mostly silicates, galactic nucleosynthesis would be required to accumulate sufficient silicon and oxygen and enable them to condense onto grains in massive AGB star winds. If they are mostly carbonaceous, stars of lower mass than $\sim 3\,M_{\odot}$ have to reach the AGB (~300 Myr) and start producing C grains, their production rate peaking when $\sim 2\,M_{\odot}$ stars reach the AGB, about 1 Gyr later. If the carriers of the UV bump are not stardust, they are produced in the general ISM on timescales of the order of 0.5 Gyr (Whittet 2003, and references therein). The dust production timescales can become significantly shorter, if SNe of type II (which could occur at very high redshift; see Liang & Li 2008; Nozawa et al. 2008) or the slow winds of their precursors (red supergiants) play a role. In any case, the carriers of the UV bump have to spread and survive across and above the disc (possibly as high as 10 kpc), where part of them (or their parent grains) are transported to speeds of 10 to $500\,\mathrm{km\,s^{-1}}$ by galactic winds and superwinds. Finally, if the presence of the carriers of the UV bump is ruled not only by their accumulation (in stars or in the ISM) but also by their survival (e.g., favoured by self-shielding; see NP05), some threshold in either dust-to-gas ratio or metal abundance may have been reached (see Gordon et al. 2003).

6. Conclusions

We have selected a total of 78 UV-luminous galaxies at $1 < z < 2.5$ with average stellar mass of about $10^{10}\,M_{\odot}$ from GMASS, a deep spectroscopic survey of IRAC $4.5\,\mu$m-flux limited galaxies at $z \sim 2$ in the GOODS-S (Kurk et al. 2008a). This sample extends to 186 the number of actively star-forming, intermediate-mass (i.e., with stellar masses of 10^{10}–$10^{11}\,M_{\odot}$) galaxies at $1 < z < 2.5$ with high S/N optical spectra and multiwavelength photometry, selected from the FDF, K20, and GDDS samples and investigated by NPPS. Its heterogeneous nature assures us that the total sample probes the population of UV-luminous, massive galaxies at these redshifts comprehensively, beyond the limitations of the selection criteria of individual samples.

The properties of the UV extinction curve, i.e., far-UV slope and presence (or absence) of the broad absorption feature centred on 2175 Å ("UV bump"), were constrained by a parametric

description of the spectra by mapping the rest-frame UV spectral energy distributions of the individual galaxies. We have interpreted the data by applying a suite of different models combining radiative transfer and stellar population synthesis. For the 68 GMASS spectra at $1.5 < z < 2.5$ in particular, additional Lorentzian-like "Drude" fitting of the UV bump was performed. The overall analysis placed constraints on the dust population of large molecules and small grains responsible for the extinction at UV wavelengths.

Hereafter, we summarise the main results of our analysis and place them in the context of our previous results.

- About 30% of the spectra of actively star-forming, intermediate-mass galaxies at $1 < z < 2.5$ undoubtedly exhibit broad absorption features centred on ~2175 Å, regardless of redshift. We term such galaxies SUBGs (*s*ignificant *U*V *b*ump *g*alaxies). Taking into account their measured UV slopes, we conclude that the extinction curves characterising these galaxies differ from those observed in the SMC, as well as from those characterising nearby starburst galaxies and typical LBGs at $2 < z < 4$.
- If attenuation at UV wavelengths is dominated by dust distributed above the stellar body of a galaxy, as suggested at least for SUBGs, effective UV extinction curves in-between those typically observed in the SMC and LMC characterise UV-luminous, intermediate-mass galaxies at $1 < z < 2.5$. This dust/star configuration originates from the action of galactic winds or localised superwinds. Stronger intrinsic UV bumps are possible for an enhanced mixing of dust and stars (probably in a disc), patchier dusty screens, age-dependent extinction effects, and significantly diverse regions in terms of star formation and dustiness within a galaxy. Since this cannot be excluded, especially for non-SUBGs (for which the ratio $L_{\rm IR}/L_{\rm UV}$ is significantly lower than expected for dust-screen dominated galaxies), the fraction of high-redshift galaxies with LMC-type extinction curves can be higher than inferred from the apparent bump strength.
- The UV bumps of the analysed UV-luminous high-redshift galaxies exhibit about 60% of the width typically found in the LMC and Milky Way. In the local Universe, similar widths are found only for some sightlines towards the supergiant shell of ionised filaments LMC 2 near 30 Dor. This suggests similar environments in terms of radiation field, dust-to-gas mass ratio, and population of dust grains and molecules.
- The presence of multiple carriers of the UV bump (probably organic carbon and amorphous silicates) in a galaxy argues that AGB stars have already started to return large amounts of dust to the ISM. The required chemical enrichment is particularly evident for GMASS SUBGs at $1.5 < z < 2.5$, for which relatively large equivalent widths can be measured for several UV absorption features, mainly of interstellar origin, produced by Si, S, C, Al, Fe, and Mg.
- SUBGs are more luminous at 8 μm (rest frame) than most of the other GMASS galaxies at $1.5 < z < 2.5$, which, on the other hand, have lower average star-formation rates. This is circumstantial evidence that carbonaceous dust has already been synthesised in relatively large amounts at these redshifts, since polycyclic aromatic hydrocarbons (which originate in AGB stars) probably dominate the emission at 8 μm.
- Large amounts of UV radiation and shocks must be present in our sample galaxies. This is particularly true for SUBGs, since their specific star-formation rates are higher. Survival of the small-size dust component in such harsh environments is helped by the higher injection rates and more efficient dust self-shielding. Consistently, UV-luminous, massive galaxies at $1 < z < 2.5$ with LMC 2-like dust suffer from higher attenuation at UV wavelengths and, according to our models, host larger amounts of dust.

The frequent occurrence of significant UV bumps in spectra of high-redshift galaxies appears to imply that these galaxy SEDs could be reproduced more accurately by models with attenuation curves that differ from the Calzetti law, which does not account for the presence of a UV bump. The investigation of the attenuation curves of star-forming, high-redshift galaxies across a wider wavelength range is deferred to a future paper. However, the present study indicates that a Calzetti law plus a Lorentzian-like bump reproduces the spectra of SUBGs at least for the wavelength range 1450−2900 Å. Accounting for the presence of a UV bump in this way involves systematic but small changes in crucial properties such as the SFR in SUBGs.

Acknowledgements. Many thanks go to David Elbaz and Benjamin Magnelli for the 70 μm stacking using the GOODS-S data of David Frayer and collaborators. DP thanks Adolf Witt for useful discussions on the carriers of the UV bump. Finally, we thank the anonymous referee for her/his helpful comments that improved this paper. The spectra of the GMASS (ESO large programme 173.A-0687), FDF, and K20 samples are based on observations obtained with FORS at the ESO VLT, Paranal, Chile. The latter spectra as well as the Hubble ACS images of the GOODS-S were retrieved from the ESO/ST-ECF Science Archive Facility. The GDDS spectra stem from observations with GMOS at the Gemini North Telescope, Mauna Kea, USA. S.N. is funded by the *Agence Nationale de la Recherche* (ANR) of France in the framework of the D-SIGALE project. J.D.K. is supported by the *Deutsche Forschungsgemeinschaft* (DFG), grant SFB-439.

References

Abraham, R. G., Glazebrook, K., McCarthy, P. J., et al. 2004, AJ, 127, 2455
Aguirre, A., Hernquist, L., Katz, N., Gardner, J., & Weinberg, D. 2001a, ApJ, 556, L11
Aguirre, A., Hernquist, L., Katz, N., Gardner, J., & Weinberg, D. 2001b, ApJ, 561, 521
Allamandola, L. J., Tielens, A. G. G. M., & Barker, J. R. 1985, ApJ, 290, L25
Allamandola, L. J., Tielens, A. G. G. M., & Barker, J. R. 1989, ApJS, 71, 733
Barsella, B., Ferrini, F., Greenberg, J. M., & Aiello, S. 1989, A&A, 209, 349
Beck, R., Carilli, C. L., Holdaway, M. A., & Klein, U. 1994, A&A, 292, 409
Bernet, M. L., Miniati, F., Lilly, S. J., Kronberg, P. P., & Dessauges-Zavadsky, M. 2008, Nature, 454, 302
Bianchi, S., & Ferrara, A. 2005, MNRAS, 358, 379
Bianchi, S., & Schneider, R. 2007, MNRAS, 378, 973
Bianchi, S., Ferrara, A., & Giovanardi, C. 1996, ApJ, 465, 127
Bolzonella, M., Miralles, J.-M., & Pelló, R. 2000, A&A, 363, 476
Bradley, J., Dai, Z. R., Erni, R., et al. 2005, Science, 307, 244
Buat, V., Iglesias-Páramo, J., Seibert, M., et al. 2005, ApJ, 619, L51
Calzetti, D., Kinney, A. L., & Storchi-Bergmann, T. 1994, ApJ, 429, 582
Calzetti, D., Armus, L., Bohlin, R. C., et al. 2000, ApJ, 533, 682
Cardelli, J. A., & Clayton, G. C. 1991, AJ, 101, 1021
Cardelli, J. A., Clayton, G. C., & Mathis, J. S. 1989, ApJ, 345, 245
Cassata, P., Cimatti, A., Franceschini, A., et al. 2005, MNRAS, 357, 903
Caulet, A., Deharveng, L., Georgelin, Y. M., & Georgelin, Y. P. 1982, A&A, 110, 185
Cimatti, A., Mignoli, M., Daddi, E., et al. 2002, A&A, 392, 395
Cimatti, A., Cassata, P., Pozzetti, L., et al. 2008, A&A, 482, 21
Clayton, G. C. 2004, in Astrophysics of dust, ed. A. N. Witt, G. C. Clayton, & B. T. Draine, ASP Conf. Ser., 309, 57
Compiégne, M., Abergel, A., Verstraete, L., & Habart, E. 2008, A&A, 491, 797
Conselice, C. J., Bershady, M. A., Dickinson, M., & Papovich, C. 2003, AJ, 126, 1183
Cowie, L. L., Songaila, A., Hu, E. M., & Cohen, J. G. 1996, AJ, 112, 839
Daddi, E., Dickinson, M., Morrison, G., et al. 2007a, ApJ, 670, 156
Daddi, E., Alexander, D. M., Dickinson, M., et al. 2007b, ApJ, 670, 173
Dale, D. A., & Helou, G. 2002, ApJ, 576, 159
Davies, J. I., Alton, P., Bianchi, S., & Trewhella, M. 1998, MNRAS, 300, 1006
Désert, F. X., Boulanger, F., & Puget, J. L. 1990, A&A, 237, 215

Dickinson, M., Giavalisco, M., & the GOODS Team 2003, in The Mass of Galaxies at Low and High Redshift, Proceedings of the ESO Workshop held in Venice 2001, ed. R. Bender, & A. Renzini, 324
Drory, N., Salvato, M., Gabasch, A., et al. 2005, ApJ, 619, L131
Elíasdóttir, Á., Fynbo, J. P. U., Hjorth, J., et al. 2008, [arXiv:0810.2897]
Erb, D. K., Shapley, A. E., Pettini, M., et al. 2006a, ApJ, 644, 813
Erb, D. K., Steidel, C. C., Shapley, A. E., et al. 2006b, ApJ, 647, 128
Ferrara, A., Aiello, S., Ferrini, F., & Barsella, B. 1990, A&A, 240, 259
Ferrara, A., Ferrini, F., Barsella, B., & Franco, J. 1991, ApJ, 381, 137
Ferrara, A., Bianchi, S., Cimatti, A., & Giovanardi, C. 1999, ApJS, 123, 437
Fitzpatrick, E. L. 2004, in Astrophysics of dust, ed. A. N. Witt, G. C. Clayton, & B. T. Draine, ASP Conf. Ser., 309, 33
Fitzpatrick, E. L., & Massa, D. 1986, ApJ, 307, 286
Fitzpatrick, E. L., & Massa, D. 1990, ApJS, 72, 163
Fitzpatrick, E. L., & Massa, D. 2007, ApJ, 663, 320
Fynbo, J., Vreeswijk, P., Jakobsson, P., et al. 2007, Msngr, 130, 43
Galliano, F., Dwek, E., & Chanial, P. 2008, ApJ, 672, 214
Gavazzi, G., & Scodeggio, M. 1996, A&A, 312, L29
Gavazzi, G., Pierini, D., & Boselli, A. 1996, A&A, 312, 397
Giavalisco, M., Ferguson, H. C., Koekemoer, A. M., et al. 2004, ApJ, 600, L93
Gordon, K. D., Clayton, G. C., Misselt, K. A., Landolt, A. U., & Wolff, M. J. 2003, ApJ, 594, 279
Greenberg, J. M., Ferrini, F., Barsella, B., & Aiello, S. 1987, Nature, 327, 214
Greggio, L., Renzini, A., & Daddi, E. 2008, MNRAS, 388, 829
Halliday, C., Daddi, E., Cimatti, A., et al. 2008, A&A, 479, 417
Heckman, T. M. 2002, in Extragalactic Gas at Low Redshift, ed. J. S. Mulchaey, & J. Stocke (San Francisco: ASP), ASP Conf. Proc., 254, 292
Heckman, T. M., Robert, C., Leitherer, C., Garnett, D. R., & van der Rydt, F. 1998, ApJ, 503, 646
Hopkins, P. F., Strauss, M. A., Hall, P. B., et al. 2004, AJ, 128, 1112
Iben, I. Jr., & Renzini, A. 1983, ARA&A, 21, 271
Jones, A. P., Tielens, A. G. G. M., Hollenbach, D. J., & McKee, C. F. 1994, ApJ, 433, 797
Kong, X., Charlot, S., Brinchmann, J., & Fall, S. M. 2004, MNRAS, 349, 769
Krühler, T., Küpcü Yoldaş, A., Greiner, J., et al. 2008, ApJ, 685, 376
Kurk, J. D., Cimatti, A., Daddi, E., et al. 2008a, in The Second Annual Spitzer Science Center Conference: Infrared Diagnostics of Galaxy Evolution, ed. R.-R. Chary, H. I. Teplitz, & K. Sheth (San Francisco: ASP), ASP Conf. Ser., 399, 303
Kurk, J., Cimatti, A.. Zamorani, G., et al. 2008b, in Panoramic Views of Galaxy Formation and Evolution, ed. T. Kodama, T. Yamada, & K. Aoki (San Francisco: ASP), ASP Conf. Ser., 399, 332
Lacy, M., Storrie-Lombardi, L. J., Sajina, A., et al. 2004, ApJS, 154, 166
Léger, A., & Puget, J. L. 1984, A&A, 137, L5
Leitherer, C., Leão, J. R. S., Heckman, T. M., et al. 2001, ApJ, 550, 724
Liang, S. L., & Li, A. 2009, ApJ, 690, L56
Luo, B., Bauer, F. E., Brandt, W. N., et al. 2008, ApJS, 179, 19
Madau, P., Ferguson, H. C., Dickinson, M. E., et al. 1996, MNRAS, 283, 1388
Maiolino, R., Marconi, A., Salvati, M., et al. 2001, A&A, 365, 28
Malhotra, S. 1997, ApJ, 488, L101
Maraston, C. 2005, MNRAS, 362, 799
Marcillac, D., Elbaz, D., Chary, R. R., et al. 2006, A&A, 451, 57
Mathis, J. S. 1994, ApJ, 422, 176
McKee, C. F. 1989, ApJ, 345, 782
Mehlert, D., Noll, S., Appenzeller, I., et al. 2002, A&A, 393, 809
Mehlert, D., Tapken, C., Appenzeller, I., et al. 2006, A&A, 455, 835
Mennella, V., Colangeli, L., Palumbo, P., et al. 1996, ApJ, 464, L191
Mennella, V., Colangeli, L., Bussoletti, E., et al. 1998, ApJ, 507, L177
Meurer, G. R., Heckman, T. M., & Calzetti, D. 1999, ApJ, 521, 64
Mignoli, M., Cimatti, A., Zamorani, G., et al. 2005, A&A, 437, 883
Misselt, K. A., Clayton, G. C., & Gordon, K. D. 1999, ApJ, 515, 128
Murray, N., Quataert, E., & Thompson, T. A. 2005, ApJ, 618, 569
Noll, S., & Pierini, D. 2005, A&A, 444, 137 (NP05)
Noll, S., Mehlert, D., Appenzeller, I., et al. 2004, A&A, 418, 885
Noll, S., Pierini, D., Pannella, M., & Savaglio, S. 2007, A&A, 472, 455 (NPPS)
Nozawa, T., Kozasa, T., Umeda, H., et al. 2008, [arXiv:0812.1448]
Panuzzo, P., Granato, G. L., Buat, V., et al. 2007, MNRAS, 375, 640
Papoular, R. J., & Papoular, R. 2009, [arXiv:0902.2637]
Peeters, E., Spoon, H. W. W., & Tielens, A. G. G. M. 2004, ApJ, 613, 986
Peng, C. Y., Ho, L. C., Impey, C. D., & Rix, H.-W. 2002, AJ, 124, 266
Pierini, D., Gordon, K. D., & Witt, A. N. 2003, RMxAC, 17, 200
Pierini, D., Maraston, C., Bender, R., & Witt, A. N. 2004a, MNRAS, 347, 1
Pierini, D., Gordon, K. D., Witt, A. N., & Madsen, G. J. 2004b, ApJ, 617, 1022
Pierini, D., Maraston, C., Gordon, K. D., & Witt, A. N. 2005, MNRAS, 363, 131
Pitman, K. M., Clayton, G. C., & Gordon, K. D. 2000, PASP, 112, 537
Pope, A., Bussmann, R. S., Dey, A., et al. 2008, ApJ, 689, 127
Pozzetti, L., & Mannucci, F. 2000, MNRAS, 317, L17
Puget, J. L., & Léger, A. 1989, ARA&A, 27, 161
Reddy, N. A., & Steidel, C. C. 2004, ApJ, 603, L13
Renzini, A. 2008, MNRAS, 391, 354
Renzini, A., & Voli, M. 1981, A&A, 94, 175
Rix, S. A., Pettini, M., Leitherer, C., et al. 2004, ApJ, 615, 98
Salpeter, E. E. 1955, ApJ, 121, 161
Savaglio, S., Glazebrook, K., Abraham, R. G., et al. 2004, ApJ, 602, 51
Sérsic, J. L. 1968, Atlas de galaxias australes (Cordoba: Observatorio Astronomico)
Shapley, A. E., Steidel, C. C., Pettini, M., & Adelberger, K. L. 2003, ApJ, 588, 65
Silva, L., Granato, G. L., Bressan, A., & Danese, L. 1998, ApJ, 509, 103
Sloan, G. C., Kraemer, K. E., Wood, P. R., et al. 2008, ApJ, 686, 1056
Sorrell, W. H. 1990, MNRAS, 243, 570
Stern, D., Eisenhardt, P., Gorjian, V., et al. 2005, ApJ, 631, 163
Teplitz, H. I., Desai, V., Armus, L., et al. 2007, ApJ, 659, 941
Tielens, A. G. G. M., Hony, S., Van Kerckhoven, C., & Peeters, E. 1999, in The Universe as Seen by ISO, ed. P. Cox, & M. F. Kessler, ESA SP-427 (Noordwijk: ESA), 579
Tielens, A. G. G. M., van Kerckhoven, C., Peeters, E., & Hony, S. 2000, in Astrochemistry: From Molecular Clouds to Planetary, ed. Y. C. Minh, & E. F. van Dishoeck (Dordrecht: Kluwer), IAU Symp., 197, 349
Valencic, L. A., Clayton, G. C., & Gordon, K. D. 2004, ApJ, 616, 912
Vanden Berk, D., Khare, P., York, D. G., et al. 2008, ApJ, 679, 239
Veilleux, S., Cecil, G., & Bland-Hawthorn, J. 2005, ARA&A, 43, 769
Vernet, J., Fosbury, R. A. E., Villar-Martín, M., et al. 2001, A&A, 366, 7
Vijh, U. P., Witt, A. N., & Gordon, K. D. 2003, ApJ, 587, 533
Wang, B., & Heckman, T. M. 1996, ApJ, 457, 645
Wang, J., Hall, P. B., Ge, J., Li, A., & Schneider, D. P. 2004, ApJ, 609, 589
Weiner, B. J., Coil, A. L., Prochaska, J. X., et al. 2009, ApJ, 692, 187
Whittet, D. C. B. 2003, Dust in the galactic environment, 2nd edn. (Bristol: Institute of Physics (IOP) Publishing)
Wild, V., & Hewett, P. C. 2005, MNRAS, 361, L30
Wisniewski, J. P., Bjorkman, K. S., Magalhães, A. M., & Pereyra, A. 2007, ApJ, 664, 296
Witt, A. N., & Gordon, K. D. 2000, ApJ, 528, 799
Wolfe, A. M., Jorgenson, R. A., Robishaw, T., Heiles, C., & Prochaska, J. X. 2008, Nature, 455, 638
Zhukovska, S., Gail, H.-P., & Trieloff, M. 2008, A&A, 479, 453